Planar faults in γ - TiAl
An atomistic study

Master Thesis

BSc. Phillip Dumitraschkewitz

Department of Physical Metallurgy and Materials Testing
Montanuniversität Leoben

Leoben, May 2015

Affidavit:
I declare in lieu of oath, that I wrote this thesis and performed the associated research myself, using only literature cited in this volume.

Date

Signature

Acknowledgements

I would like to thank Ass.Prof. Dr. Svea Mayer and her intermetallics working group for such a friendly working environment, the possibility to participate and get insight in a scientific research group. I wish to express my sincere thanks to Univ.-Prof. Dr. Helmut Clemens, head of the Department, for the possibility to write my master thesis at this well-respected department.
I would like to express my gratitude to my supervisor Dr. David Holec for his engagement and guidance through this thesis. Especially I would like to thank him for the patience proofreading the thesis and the help with the LaTeX.
Also I would like to thank Prof. Dr. Jörg Neugebauer and his division at the MPIE for running part of the calculations on their cluster in Düsseldorf.
I would like to thank my parents for giving me the possibility to graduate at the university. I am also grateful to my family and friends for helping me in all circumstances and who walked with me this journey over the last years.

Contents

List of symbols and abbreviations

A	area
ALCHEMI	atom location channeling enhanced microanalysis
APB	antiphase boundary
APT	atomic probe tomography
B_0	bulk modulus
$B_{0,p}$	bulk modulus derivative with respect to the pressure, for pressure = 0
$\vec{b}$, b	Burgers vector and its length
$\vec{b}_s$, $\vec{b}_e$	screw and edge Burgers vectors
$\vec{b}_{\text{twin}}$	twinning partial Burgers vector
C_{ij}	elastic constants
CSF	complex stacking fault
DFT	density functional theory
E	energy
e	elementary charge
ϵ_0	vacuum permittivity
EAM	embedded atom method
EDS	energy dispersive X-ray spectroscopy
EELS	electron energy loss spectroscopy
ESF	extrinsic stacking fault
EoS	equation of state
$\vec{\eta}_1$	shear direction
$\vec{F}$	force
FLAPW	full-potential linearized augmented plane wave
FP-LMTO	full-potential linear muffin-tin orbital
γ	stacking fault energy
GGA	generalized gradient approximation
GSFE	generalized stacking fault energy
GPFE	generalized planar fault energy
$\hbar$	reduced Planck constant
$\hat{H}$	Hamiltonian (operator)

K_1, K_2	first and second undistorted plane
LAMMPS	Large-scale Atomic/Molecular Massively Parallel Simulator
LAPW	linear augmented plane waves
LDA	local density approximation
LKKR-CPA	layer Korringa-Kohn-Rostoker coherent potential approximation
LOM	light-optical microscope
m_e	electron mass
MD	Molecular Dynamics
n	number of planes in the supercell
ν	Poisson's ratio
∇	nabla operator
∇^2	Laplace operator
$\vec{p}$	momentum
PAW	projector augmented wave method
PBE	Perdew, Burke and Ernzerhof
PBC	periodic boundary condition
PW91	Perdew-Wang-91
Ψ	many-electron wave function
$\vec{r}$	position
r_e	partial dislocation separation
$\rho(\vec{r})$	electron density
S	plane of shear
SEM	scanning electron microscope
SESF	superlattice extrinsic stacking fault
SFE	stacking fault energy
SISF	superlattice intrinsic stacking fault
SQS	special quasi-random structure
t	time
$\hat{T}$	operator of the kinetic energy
$\tau_{\text{crit.}}$	critical twinning stress
TEM	transmission electron microscopy
V_0	equilibrium volume
$\hat{V}$	operator corresponding to (various) potentials
V_{ex}	exchange-correlation potential
UPP	ultrasoft pseudo potentials
VASP	Vienna Ab initio Simulation Package
WB	weak beam transmission electron microscopy
$\vec{\xi}$	dislocation line direction
Z	atomic number

Abstract/Kurzfassung

Abstract

In this Master Thesis two different methodologies for building atomic models of planar faults in γ-TiAl are implemented. The generalized stacking fault energy for stoichiometric TiAl is calculated within the framework of Density Functional Theory and Molecular Dynamics with the code packages VASP and LAMMPS, respectively. Different energy profiles corresponding to different dislocation dissociation schemes are discussed. The impact on the stacking fault energies for different relaxation methods, varying cell volume and using different exchange correlation potentials is examined. A simple model is implemented to get trends for different alloying elements. The most striking results are that the stacking fault energies depend on the chosen relaxation method due to the fact that their energy minimum do not lie exactly on their hard-sphere model positions and that the ratio $\frac{\mathrm{Ti+X}}{\mathrm{Al}}$ has a huge impact, generally finding lower stacking fault energy values for ratios bigger than 1.

Kurzfassung

In dieser Masterarbeit wurden zwei verschiedene Methoden um die atomaren Modelle der planaren Fehler in γ-TiAl zu implementieren angewandt. Die generalisierte Stapelfehlerenergie für stöchiometrisches TiAl wurde mit Hilfe der Dichtefunktionaltherorie und Molekulardynamik mit den entsprechenden Codes VASP und LAMMPS berechnet. Verschiedene Energieprofile, welche zu verschiedenen Versetzungsaufspaltungen gehören, wurden behandelt. Des Weiteren wurde der Einfluss von verschiedenen Relaxations-Methoden, variierten Einheitszellvolumen und verschiedenen Austausch-Korrelationspotentialen auf die Stapelfehlerenergie untersucht. Ein einfaches Modell zur Untersuchung des Einflusses von Legierungselementen wurde implementiert. Die herausragendsten Ergebnisse sind, dass die Stapelfehlerenergien von der gewählten Relaxationsart abhängen, aufgrund der Tatsache, dass deren wirkliche Energieminima nicht an den Kugelmodell-Positionen liegen, und das Verhältnis $\frac{\mathrm{Ti+X}}{\mathrm{Al}}$ einen großen Einfluss auf sie hat. Für $\frac{\mathrm{Ti+X}}{\mathrm{Al}}$-Verhältnisse größer als 1 wurden generell kleinere

Stapelfehlerenergien gefunden.

Chapter 1

Introduction

Today, intermetallic Titanium Aluminides are materials already in use. Their applications range from low-pressure turbine blade materials in the aircraft industry to turbo charger wheels and valves in the automotive industry [1]. Their outstanding properties include low density, high specific strength, high specific stiffness, and good creep properties up to 750 °C. Additionally, their good oxidation behavior and burn resistance in comparison with titanium alloys, is an advantage [2]. In contrast to ceramic materials, Titanium Aluminides also exhibit the ability to plastically deform at room temperature [3].
The state of the art TiAl alloys consist of an α_2 (Ti_3Al) phase, a γ (TiAl) phase, a β/B2 phase, and possibly additional phases [4]. The main constituent is the γ-TiAl phase which fundamentally influences the alloy properties in its as-used state.

The γ-TiAl phase has an $L1_0$ structure, which is closely related to a tetragonally strained ordered fcc lattice. Therefore, the topic of stacking faults can be treated similar to a fcc metal. In general, a stacking fault in an fcc lattice is a deviation from the normal stacking sequence "ABCABC..." of the (111) planes [4, 5].
The stacking fault energy has a huge impact on the plastic deformation behavior of fcc metals. It determines the spreading of dissociated partial dislocations, and therefore influences the cross-slip properties of screw dislocations. It is observed that metals with smaller stacking fault energies exhibit more mechanical twinning which can be an additional deformation mechanism [6, 7].
The stacking fault energy is not directly obtainable in experiment as it is only possible to measure the separation of partial dislocations. The experimental measurements are time consuming since transmission electron microscopy (TEM) is needed, and sample preparation can be difficult. Hence, a theoretical study of stacking fault energies is a reasonable alternative to examine stacking faults, and it is often applied today.

The aim of the present study is to investigate stacking fault energies and planar faults

in γ-TiAl via *ab initio* and Molecular Dynamics approaches using the VASP (*ab initio*) and LAMMPS (Molecular Dynamics) codes. The main focus is put on building up of a methodology for calculating the stacking fault energies. Additional points include an investigation on deformation-relevant quantities, and a study of the impact of ternary alloying elements on the γ-TiAl phase.

Chapter 2

TiAl-based alloys and their planar faults

2.1 Crystallography

The $L1_0$ structure of the γ-TiAl phase (Fig. 2.1) is an ordered tetragonally strained fcc structure with alternating occupation of the (002) planes. The c/a-ratio of the $L1_0$ structure for TiAl is greater than 1 which is unusual for this structure; the intermetallic compounds CdPd, AuCd, MnPt, NbIr all show c/a ratios smaller than 1, only AgTi exhibits $c/a \sim 1$ [8]. The experimental lattice constants of stoichiometric γ-TiAl are $a = 0.3999\,\text{nm}$ and $c = 0.4077\,\text{nm}$, thus $c/a = 1.02$ [4].
The close-packed [110], [101] and [011] directions are crystallographically not equivalent due to the fact that the cell is ordered and tetragonally stretched in the $\vec{c}$ direction. Consequently the Miller notation has been modified to mixed parenthesis $\langle uvw]$ for directions and $\{hkl)$ for planes to differentiate the first two equivalent indices from the third on. This means that the first two indices can be permuted while the third index is fixed [4, 9].

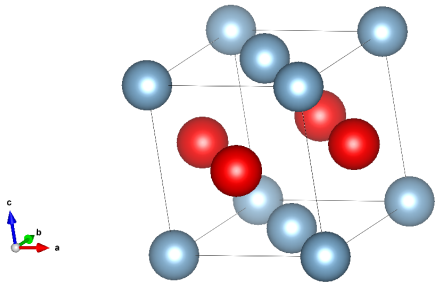

Figure 2.1: A conventional unit cell of the $L1_0$ structure(red and blue spheres denote Ti and Al atoms, respectively)

The other important bulk phases in titanium aluminide alloys are the α_2 (Ti_3Al) and the β/B2 TiAl phase. The α_2 (Ti_3Al) phase has the $D0_{19}$ structure which is an ordered hexagonal structure. The β/B2 TiAl phase has the bcc lattice and the ordered form of it is the B2

structure (CsCl prototype) [4]. The latter phase plays an important role in the alloying concept of the TNM alloys [1, 2].

2.2 Microstructure and technical alloys

The commonly used TiAl-alloys exhibit four different important in-use microstructures: a fully lamellar, a nearly lamellar, a duplex, and a near gamma microstructure. The coarse grained fully lamellar and the nearly lamellar microstructure show good creep and fracture toughness behavior, but low tensile plastic elongation capability at the room temperature. On the other hand, the fine-grained equiaxed nearly gamma and the duplex structures show lower fracture toughness and creep resistance but moderate tensile ductility at ambient temperatures **??**.

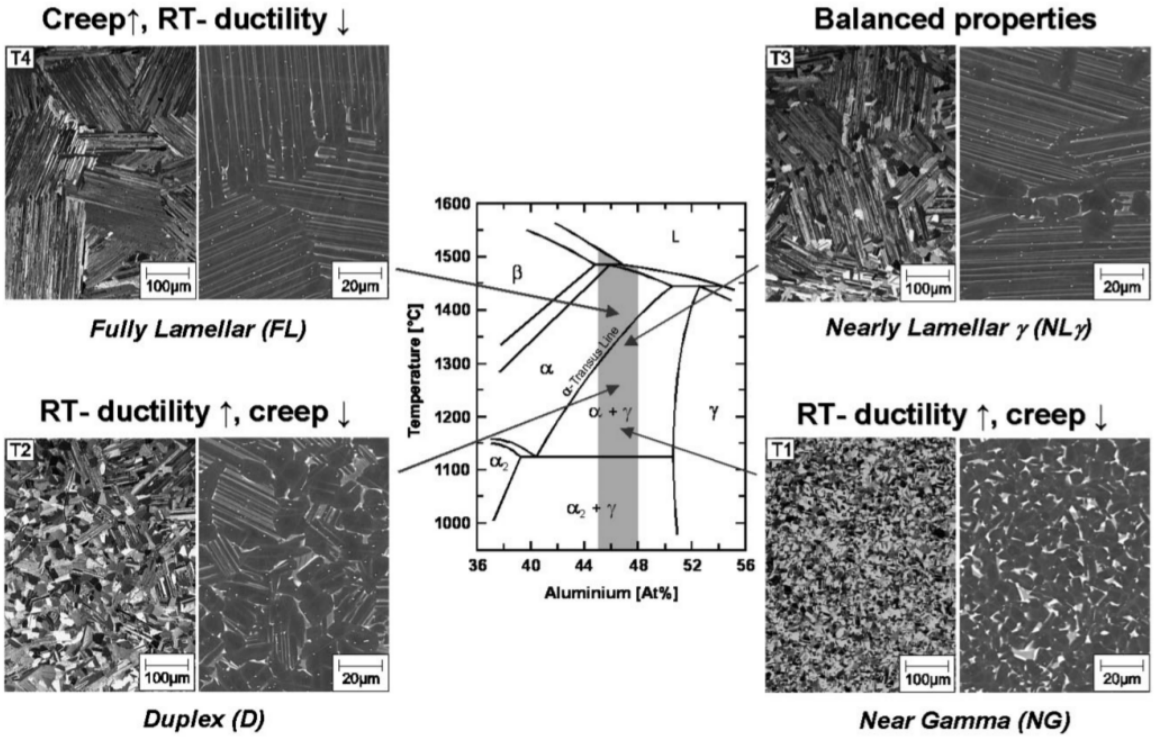

Figure 2.2: Microstructural types: left half of the micrographs are light-optical microscope (LOM) images, the right half are scanning electron images (SEM) in back scattered electron (BSE) contrast [2, 10]. Desired microstructure can be obtained by adjusting the annealing temperature and holding time before cooling, and by varying the cooling rate in the cooling process.

The appearance of the microstructure depends on the alloy chemistry and applied heat treatment route as shown in Fig. 2.2. The fully lamellar type consists of grains containing α_2/γ colonies. The nearly gamma microstructure consists of globular γ-TiAl grains and small amounts of α_2-Ti_3Al situated at triple points. The duplex microstructure has grains with

globular γ-TiAl and grains with α_2/γ colonies. The nearly lamellar is in between the fully lamellar and the duplex microstructures with significantly smaller amount of the γ-TiAl grains [2].

Technical γ-TiAl-based materials all have Al lean compositions. The binary Ti-Al phase diagram shown in Fig. 2.3 suggests that their equilibrium constitution at room temperature is a mixture of α_2 and γ.

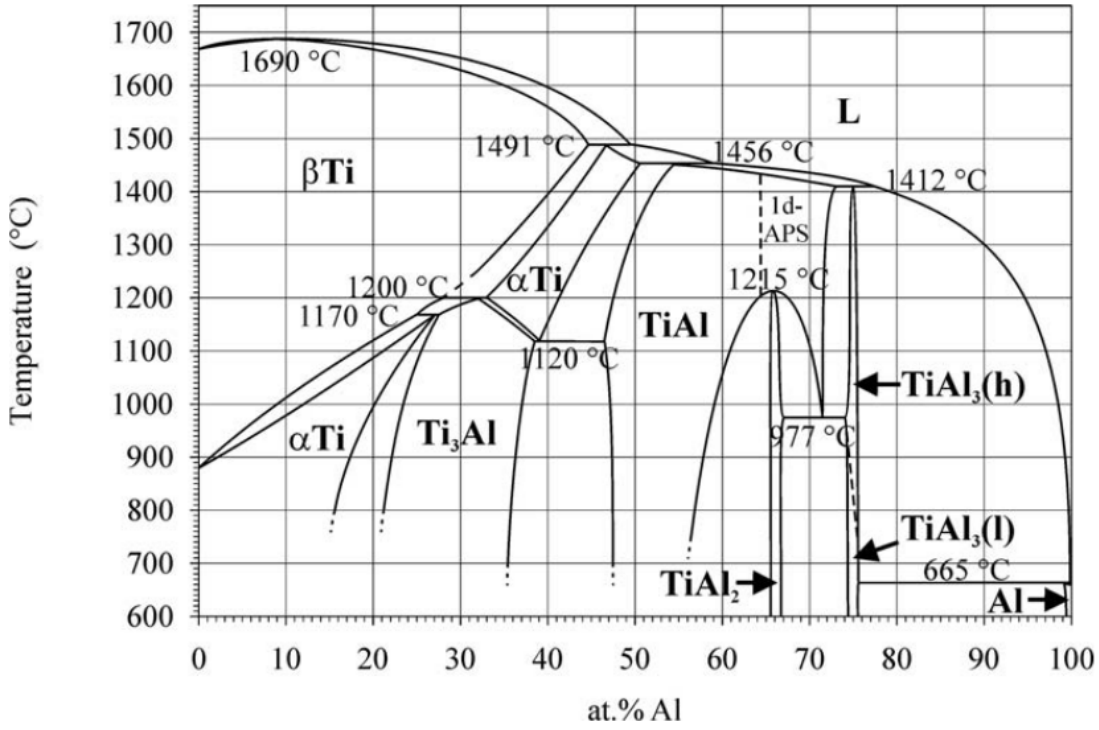

Figure 2.3: Binary phase diagram of the Ti-Al system [11].

The third generation alloys do have chemical compositions in the range of [2]:

$$\mathrm{Ti} - (42-48)\mathrm{Al} - (0-10)\mathrm{X} - (0-3)\mathrm{Y} - (0-1)\mathrm{Z} - (0-0.5)\mathrm{RE}, \tag{2.1}$$

where X= Cr, Mn, Nb, Ta; Y=Mo, W, Hf, Zr; Z=C, B, Si and RE are rare earth elements. The addition of alloying elements modifies the phase fields, so that additional phases may occur. Nb and Mo are β/B2-stabilizing elements which can lead also to fractions of an ω phase. The ω phase is unwanted because it causes embrittlement. B, Si and C can build borides, silicides and carbides, respectively, but exact form of occurrence depends on the overall alloying composition. For example, C is reported to act as a solid solution hardening agent or to build precipitates, but it is also known to change transformation properties of the alloy, such as the refinement effect on the α_2/γ lamellae. Nb slows down diffusion processes

and enhances the oxide layer properties. Ta, W and Mo improve the creep strength, however, Mo and W have negative effects on the oxidation behavior. Alloys containing Hf, Zr and rare earth elements are not yet in technical application [2].

The alloying elements can alter the the boundaries of the phase fields in a quasi binary cut diagram so that equilibrium concentration with respect to Ti and Al content in the γ-TiAl is changed. Fig. 2.4 shows the influence of adding 8 a% Nb: the equilibrium concentration of Al in the γ-TiAl decreases. Examples of the 3rd generation TiAl alloys are the so-called TNB and TNM alloys [2].

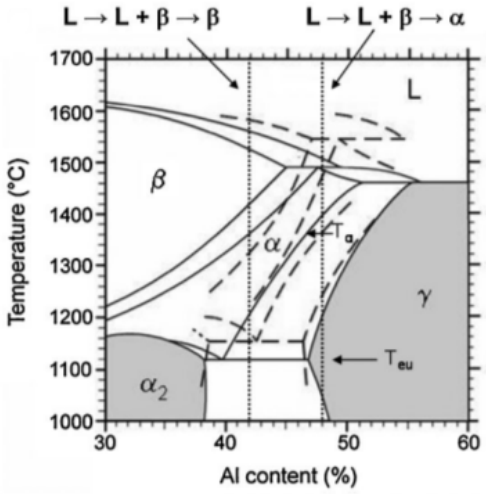

Figure 2.4: The effect of Nb on the binary Ti-Al phase diagram (full and dashed lines correspond to 0 at.% and 8 at.% Nb respectively [12].

2.3 Stacking faults and planar faults

2.3.1 The fcc lattice

Fcc and the hcp structures can be generated by different stacking of the same closed-packed planes on top of each other. The closed-packed layers in the fcc and hcp structure are the {111} and the {0001} planes, respectively. Let "A" denote the first layer, "B" the second layer, and let "C" be the third possible arrangement. When stacking the third layer over two already stacked layers, there are two different possibilities where to place the third layer, as demonstrated in the [111] projection in Fig. 2.5. One possibility is to place the third layer in a region which no hard sphere occupies yet; then the position becomes distinguishable from the other two positions. The second possibility is to put it over the projection of the "A" layer so the third layer becomes again the "A" layer. The last possibility is to place the third layer on a "B" position; this however fails to build a closed-packed structure. The stacking of sequence "ABCABC..." generates the fcc structure, while the sequence "ABAB..." generates

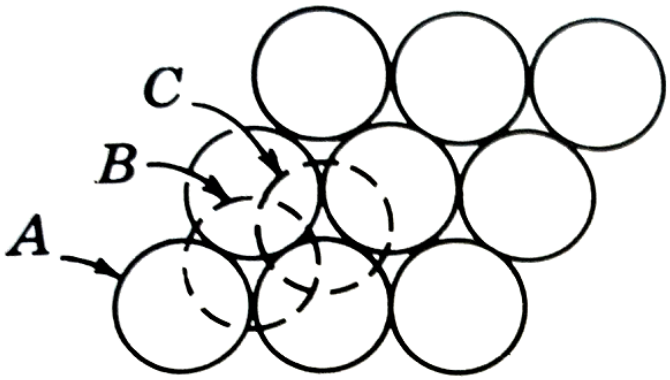

Figure 2.5: Stacking positions in close-packed structures in the [111] projection [5].

the hcp structure. In the fcc structure the {111} planes are also the glide planes and the coherent twin planes. Twins can be described by a mirror reflection with an {111} layer as a mirror plane. With the "ABC"-notation the twin can easily be described as:

$$ABCABCAB\overset{|}{C}BACBACBAC. \tag{2.2}$$

Other deviations from the stacking sequence "ABCABC..." of {111} are called stacking faults. There are two different types of stacking faults in the fcc lattice, the intrinsic and the extrinsic stacking fault. The stacking sequence is maintained on either side of the fault plane until the fault plane is reached. In the stacking sequence corresponding to the intrinsic stacking fault, there is a layer "missing":

$$ABCABC|BCABC. \tag{2.3}$$

On the contrary the extrinsic stacking fault can be seen as an inserted plane in the stacking sequence:

$$ABCAB\overset{|}{C}|B|\overset{|}{A}BCABC. \tag{2.4}$$

This fault is equivalent to two twin planes separated by two atomic layers.
Stacking faults can be produced through shearing operations on the {111} planes. When the upper half of a crystal is sheared by a distinct vector, for example for the fcc lattice by a vector $1/6[\bar{2}11]$, the planes undergo a transition $A \to B$, $B \to C$ and $C \to A$ relative to a fixed coordinate system of the bottom half of the crystal. So the starting sequence:

$$ABCA|BCABCABC \tag{2.5}$$

becomes:

$$ABCA|CABCABCA \tag{2.6}$$

producing the intrinsic stacking fault. If the planes above the fault plane, except for the first "C" plane next to the fault, get sheared again by the same vector the following sequence is generated:

$$ABCA|C|BCABCAB \tag{2.7}$$

This way an extrinsic stacking fault is generated. Applying this scheme repeating produces a coherent twin [5].

Using a simple neighbor model approximating the interaction with a central force potential, and comparing energies of different stacking sequences, approximation for the relations in between different stacking fault energies can be given [5]. It is concluded that the coherent twin boundary energy is approximately half the intrinsic stacking fault energy:

$$\gamma_{\mathrm{ISF}} \sim 2\gamma_{\mathrm{T}}. \tag{2.8}$$

The intrinsic stacking fault energy and the extrinsic stacking fault energy are nearly the same:

$$\gamma_{\mathrm{ISF}} \sim \gamma_{\mathrm{ESF}} \tag{2.9}$$

and the twin energy is about the energy needed to transform to the hcp lattice:

$$\gamma_{\mathrm{T}} \sim \gamma_{\mathrm{H}} \tag{2.10}$$

2.3.2 The $L1_0$ structure

The $L1_0$ structure of the γ-TiAl can be treated in a similar way since it can also be built from a stacking sequence "ABCABC..." of closed-packed (111) planes 2.6. Differences to the fcc lattice arise due to the ordering of the $L1_0$ structure and its tetragonality. Applying the hard sphere model on the (111) plane, the displacement of the upper part of a perfect crystal with any of the three vectors $1/6[\bar{2}11]$, $1/6[11\bar{2}]$ and $1/6[1\bar{2}1]$ produces an intrinsic stacking fault in the fcc lattice, while for the $L1_0$ structure only a displacement by the vector $1/6[11\bar{2}]$ produces a stacking fault where the nearest neighbor coordination is not destroyed. The fault generated by this $\vec{b}_3 = 1/6[11\bar{2}]$ vector is called a superlattice intrinsic stacking fault (SISF) and is shown in Fig. 2.7. The other two fault vectors $\vec{b}_1 = 1/6[\bar{2}11]$ and $\vec{b}_2 = 1/6[\bar{2}11]$ are altering the chemical environment of the atoms in the plane, the created fault is called a complex stacking fault (CSF) and is shown in Fig. 2.8. Assuming a stacking "ABC" of three layers, and only the "C" layer gets shifted by the distinct fault vector, the positions of the atoms of the "C" layer get shifted over the positions of the "A" layer atoms in a [111] projection. The occupation now for the "C" layer changes, the position of a projected "A"

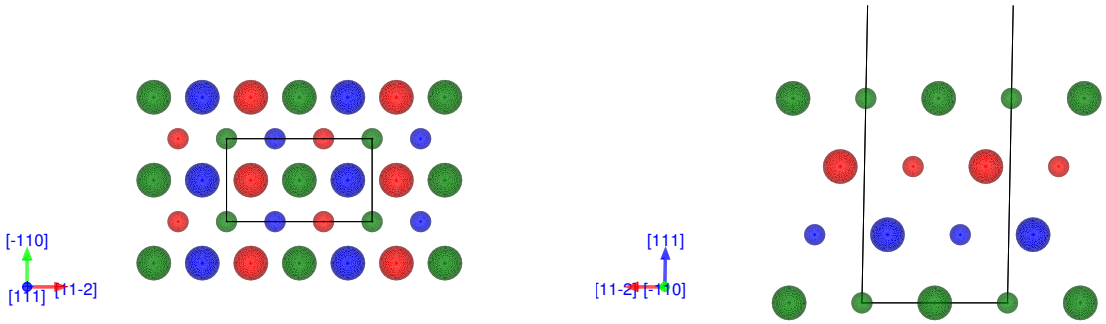

Figure 2.6: Pattern of TiAl {111} planes, same colors mean the same plane different radii of atoms indicate different element. The color sequence of the shown "ABCA" layers is green/blue/red/green.

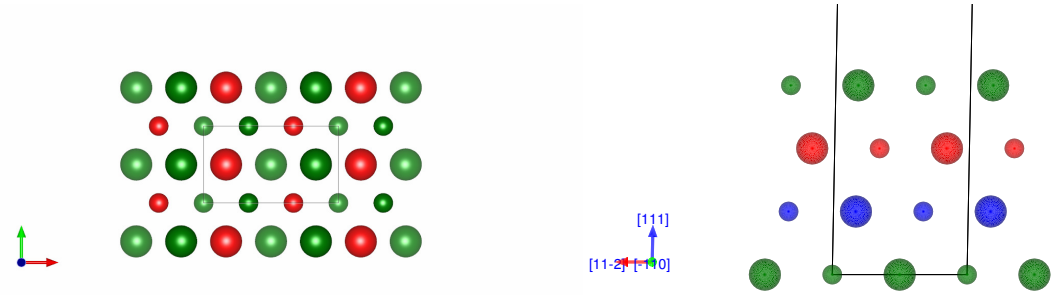

(a) The [111] projection, 4th layer overlays (green) the second blue plane.

(b) The [$\bar{1}$10] projection.

Figure 2.7: Superlattice intrinsic stacking fault pattern "ABCB".

layer Ti atom gets occupied by a "C" layer Al atom and vice versa. It should be mentioned that the vectors $\vec{b}_1$ and $\vec{b}_2$ in contrast to the $\vec{b}_3$ vector are not only producing different stacking faults, but also have a different length, caused by the tetragonality of the crystal.
Another planar fault can be created in this way of displacing a part of the perfect crystal by a vector of $\vec{b}_4 = 1/2[01\bar{1}]$. This fault is called an antiphase boundary and can be seen in Fig. 2.9. The vector $\vec{b}_4$ restores the perfect crystal in the fcc lattice, which is not the case for the $L1_0$ structure. The stacking positions do not get changed through this displacement, but Ti positions are now occupied with Al atoms and vice versa in the sheared plane [4]. Consequently the CSF can be seen as a combination of APB and SISF, a SISF with an inverted occupation.
The CSF and the SISF are specific to the {111} planes, unlike the APB. For the γ-TiAl, the {111} and the {010) are the most important ones.

Also the extrinsic stacking fault, here called the superlattice extrinsic stacking fault (SESF), and twins exist in the $L1_0$ structure. They obey the same restrictions as for the SISF. There exists only a true twin direction for a distinct {111} plane [4]. Further different γ/γ

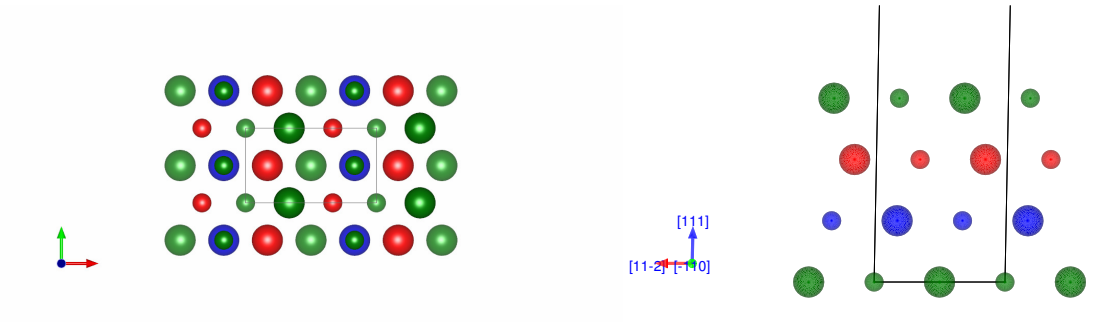

(a) The [111] projection. (b) The $[\bar{1}10]$ projection.

Figure 2.8: Complex stacking fault patterns.

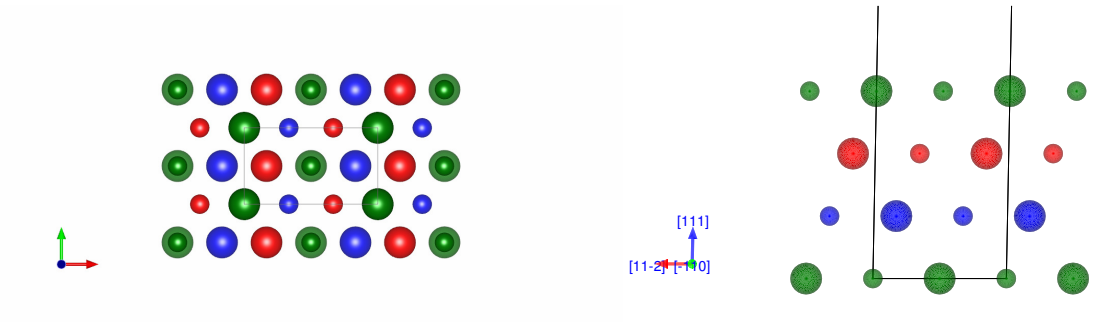

(a) The [111] projection. (b) The $[\bar{1}10]$ projection.

Figure 2.9: Antiphase boundary patterns.

interfaces can occur in the γ-TiAl: The pseudotwin variants are mutually misoriented by 60 °, the atomic stacking of the parent fcc lattice is reversed at the pseudotwin interface and the order is rotated. In the 120 ° rotational fault, the "ABC..." fcc stacking is maintained, when one neglects the tetragonality of the crystal. The true twin boundary can be created by a 180 ° rotation of the upper half of a perfect crystal. Only the stacking sequence of the $L1_0$ structure is altered similarly to the SISF and SESF. [4]

2.4 Deformation mechanisms

2.4.1 Partial dislocations in the fcc lattice

The fcc glide systems are the $\langle 110 \rangle \{111\}$. Considering again the hard-sphere model of closed-packed (111) planes, and displacing an upper half of the crystal against the bottom half along the direction $\vec{b} = 1/2[\bar{1}01]$, one will observe a larger displacement normal to the closed packed planes during the movement than when moving the planes along $\vec{b}_1 = 1/6[\bar{2}11]$ and subsequently along $\vec{b}_2 = 1/6[\bar{1}\bar{1}2]$, so that the latter path should be favored. The local arrangement generated by the displacement of $\vec{b}_1 = 1/6[\bar{2}11]$ is equal to the intrinsic stacking fault. The displacement $\vec{b}_2 = 1/6[\bar{1}\bar{1}2]$ restores again the crystal symmetry. The

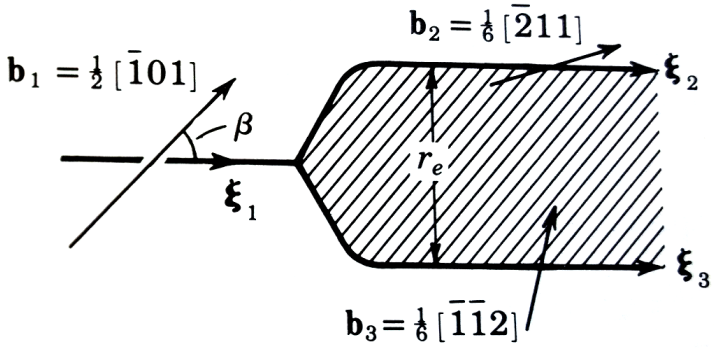

Figure 2.10: Dissociated dislocation bounding an intrinsic stacking fault (hatched area), $\vec{b}_1$ is the Burgers vector of the perfect dislocation, $\vec{b}_2$ and $\vec{b}_3$ are partials. The corresponding $\vec{\xi}_i$ are the line directions [5].

same consideration is true for dislocations, the perfect dislocation with the Burgers vector of $\vec{b}$ can split up into two partial dislocations $\vec{b}_1$ and $\vec{b}_2$. Partial dislocations of the type $1/6\langle 112\rangle$ are called Shockley partials. The partial dislocations can enclose a fault plane in between them (the intrinsic stacking fault), and are then separated by the fault plane. The dissociated dislocations repel each other by elastic forces, but their separation length is limited due to the fact that energy is needed to create the fault area between them. The equilibrium condition yield a relation between the distance of the partial dislocation distance and the stacking fault energy. Assuming isotropic behavior one gets [5]:

$$\gamma_{\mathrm{ISF}} = \frac{\mu}{2\pi r_e}\left[(\vec{b}_2 \cdot \vec{\xi}_2)(\vec{b}_3 \cdot \vec{\xi}_3) + \frac{(\vec{b}_2 \times \vec{\xi}_2)(\vec{b}_3 \times \vec{\xi}_3)}{1-\nu}\right], \tag{2.11}$$

where ν is the Poisson's ratio, r_e the partial dislocation separation, μ is the shear modulus, $\vec{b}_i$ are the Burgers vectors of the partial dislocations, and the $\vec{\xi}_i$ the dislocation line directions [5]. A model of a dissociated dislocation is shown in Fig. 2.10.

It should be noted that dynamical as well as static effects can change the partial dislocation distance r_e, e.g., when taking into account moving partials and pinned partials. Even the radii of curvature of the two partial lines can be different [5].

2.4.2 Dislocations in γ-TiAl

The most favorable slip systems should be the closed-packed lattice planes and the shortest translation vectors in these planes. Hence, in γ-TiAl the dislocations glide on the $\{111\}$ planes, and their preferred Burgers vectors are directions $\langle 110\rangle$. The Burgers vector must be a lattice translation vector. Due to the reduced symmetry of γ-TiAl in comparison to the fcc lattice, the glide direction for a perfect dislocation must be, e.g., the $[\bar{1}01]$ instead

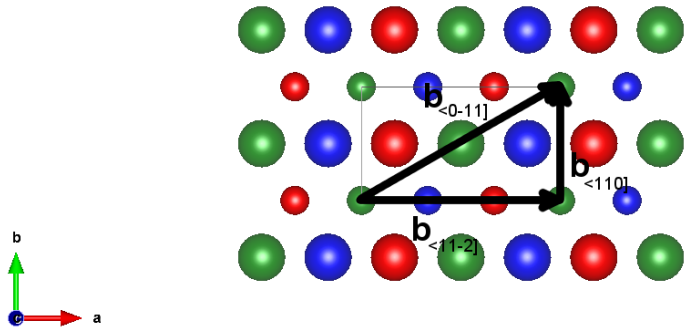

Figure 2.11: (111) planes with Burgers vectors discussed in the text.

of the $1/2[\bar{1}01]$ vector. In contrast the $\vec{b}_{\langle 110]} = 1/2\langle 1\bar{1}0]$ Burgers vector defines the same dislocation as in the fcc case, so dislocations with this Burgers vector are referred to as ordinary dislocations. The directions involving $\vec{c}$ direction, i.e. the Burgers vectors $\vec{b}_{\langle 0\bar{1}1]} = \langle 0\bar{1}1]$ and $\vec{b}_{\langle 11\bar{2}]} = 1/2\langle 11\bar{2}]$ are thought of to dissociate usually with also building an APB in between their bounding partials and are therefore referred to as the superdislocation directions [4]. The other two $\vec{b}_{\langle 1\bar{2}1]} = 1/2\langle 1\bar{2}1]$ directions are not translation vectors in the $L1_0$ structure but lead to the formation of an APB.

Screw dislocations have their Burgers vectors parallel to the the line direction. In principle, they can glide on every plane that intersects the dislocation line. Cross-slip is the change of the gliding plane of a screw dislocation. It is of importance in deformation, work hardening, creep and recovery. Cross-gliding planes for dislocations are usually closed-packed or relatively closed-packed planes that intersect the primary gliding and have the common direction [4, 5].

Dislocations in γ-TiAl can dissociate in partial dislocations bounding faults in between them, according to Frank's energy criterion. Instead of only one now three planar faults need to be considered as possible faults when dislocations dissociate. Several dislocation dissociation reactions have been proposed:

- for the ordinary dislocations the following dissociation reaction has been considered:

$$1/2[\bar{1}10] \rightarrow 1/6[\bar{2}11] + \mathrm{CSF} + 1/6[\bar{1}2\bar{1}] \tag{2.12}$$

- for the $b_{\langle 0\bar{1}1]} = \langle 0\bar{1}1]$ several dissociation reactions have been proposed [4, 13]:

$$[0\bar{1}1] \rightarrow 1/2[01\bar{1}] + \text{APB} + 1/2[01\bar{1}] \tag{2.13}$$
$$[0\bar{1}1] \rightarrow 1/6[11\bar{2}] + \text{SISF} + 1/6[\bar{1}2\bar{1}] + \text{APB} + 1/6[11\bar{2}] + \text{CSF} + 1/6[\bar{1}2\bar{1}] \tag{2.14}$$
$$[0\bar{1}1] \rightarrow 1/6[11\bar{2}] + \text{SISF} + 1/6[\bar{1}2\bar{1}] + \text{APB} + 1/2[01\bar{1}] \tag{2.15}$$
$$[0\bar{1}1] \rightarrow 1/6[11\bar{2}] + \text{SISF} + 1/6[\bar{1}54] \tag{2.16}$$
$$[0\bar{1}1] \rightarrow 1/6[11\bar{2}] + \text{SISF} + 1/2[01\bar{1}] + \text{CSF} + 1/6[\bar{1}2\bar{1}] \tag{2.17}$$

- for the $b_{\langle 11\bar{2}]} = 1/2\langle 11\bar{2}]$ dislocation [4]:

$$1/2[11\bar{2}] \rightarrow 1/2[10\bar{1}] + \text{APB} + 1/2[01\bar{1}] \tag{2.18}$$
$$1/2[11\bar{2}] \rightarrow 1/6[11\bar{2}] + \text{SISF} + 1/6[2\bar{1}\bar{1}] + \text{APB} + 1/6[11\bar{2}] + \text{CSF} + 1/6[\bar{1}2\bar{1}] \tag{2.19}$$
$$1/2[11\bar{2}] \rightarrow 1/6[11\bar{2}] + \text{SISF} + 1/6[2\bar{1}\bar{1}] + \text{APB} + 1/2[01\bar{1}] \tag{2.20}$$
$$1/2[11\bar{2}] \rightarrow 1/6[11\bar{2}] + \text{SISF} + 1/3[11\bar{2}] \tag{2.21}$$

Additionally several non-planar dissociations have been proposed but will not be discussed in this thesis. The interested reader is referred to [4].

2.4.3 Mechanical twinning in γ-TiAl

"Twinning is a particularly important deformation mechanism in crystals with only a limited number of slip systems" [5]. In general, a polycrystal needs five independent slip systems in order to plastically deform (Mises criterion). Twinning can contribute as a glide system to fulfill this condition. In higher symmetry crystals, such as bcc and fcc, twinning is observed at lower temperatures. There are two types of twinning: deformation twinning and growth twins generated by heat treatment. Here we focus on the deformation twins [5].
The geometrical aspects of twinning are usually represented by parameters K_1, K_2, S, $\vec{\eta}_1$ and $\vec{\eta}_2$ as shown in Fig. 2.12. The plane S, which contains the $\vec{\eta}_1$ direction and the normal of the K_1, is called the plane of shear. During twinning, all the points above K_1 are displaced in the direction $e\vec{\eta}_1$, where e is proportional to the distance above the K_1 plane. ψ is the acute angle between the directions $\vec{\eta}_1$ and $\vec{\eta}_2$, and therefore $g = 2\cot(\psi)$ is the shear that occurs in the twinned state. K_1 is called the undistorted plane or the twin plane. The plane K_2 is perpendicular to the shear plane S, and is deflected from K_1 by equal angles before and after shear. K_2 is also undistorted and therefore called the second undistorted plane. Mechanical twinning reproduces the crystal structure in a particular new orientation, and involves a fixed amount of shear specific to the to the crystal structure. If the shear plane S and the shear g are the same but K_1 is interchanged with K_2 as are $\vec{\eta}_1$ with $\vec{\eta}_2$ the twinning modes are said to be conjugate. Often K_1 and K_2 are equivalent planes due to higher symmetry metal crystals. A conjugate twinning system can be defined as K_1 and $-\vec{\eta}_1$, which describes

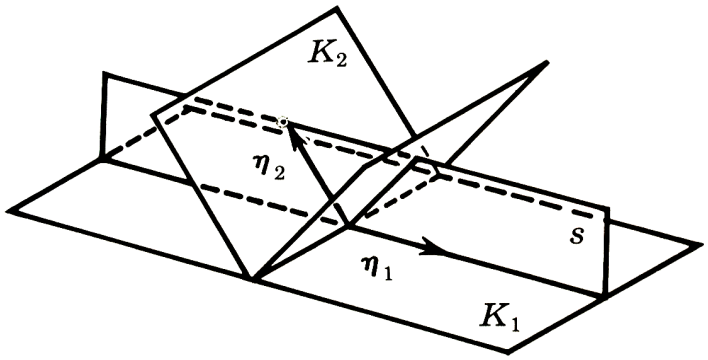

Figure 2.12: Geometrical aspects of twins: K_1 and K_2 are respectively the first and the second undistorted plane, S is the plane of shear, $\vec{\eta}_1$ is the shear direction and $\vec{\eta}_2$ lies along the intersection of K_2 and S [5].

a shear in the reverse direction. The primary twinning modes in $L1_0$ are called true twins due to the fact that they restore the crystal ordering [4, 5]. The build-up of the true twins has already been mentioned in the section 2.3.
The parameters for the true twinning are the following: $K_1 = (111)$, $K_2 = (11\bar{1})$, $\vec{\eta}_1 = 1/2[11\bar{2}]$ and $\vec{\eta}_2 = 1/2[112]$. For the conjugate mode, the parameters are: $K_1 = (111)$, $K_2 = (001)$, $\vec{\eta}_1 = 1/2[\bar{1}\bar{1}2]$ and $\vec{\eta}_2 = 1/2[110]$ [8]. The conjugate or antitwinning are unlikely to appear because they have to overcome the high energy stacking "AA" [4].
The fact that there are only four true twinning systems in the $L1_0$ structure, possesses a restriction on possible twinning modes in γ-TiAl. Consequently there exist crystal orientation/loading direction combinations which hinder the deformation twinning. The reader is referred to [4] for more details.

2.5 Literature findings regarding planar faults

Several studies have been carried out to investigate planar fault energies in γ-TiAl. Both, theoretical methods and experimental measurements have been applied. A short overview of the theoretical studies for stoichiometric γ-TiAl is given in Tab. 2.1.

The main differences between the applied theoretical studies is the build up of the supercells, the different exchange correlation potentials, and the different pseudo potentials for the wave functions (e.g., the ultrasoft pseudo potentials in [17] in contrast to the projector augmented wave method in [15]). Additionally different lattice constants and differences in cut-off energies, k-point mesh density and convergence settings contribute to discrepancies for the different DFT calculations. Nevertheless, they all predict the same energy hierarchy of the planar faults: $APB(111) > CSF > SISF$.
Some experimentally found values for near stoichiometric binary alloys are represented in Tab. 2.2. Comparing the experimental values with the calculated *ab initio* data yields that

the experimental values are generally smaller. Especially for the APB(111), the calculated values are by factor 2.5 larger. It was found that the $[01\bar{1}]$ superdislocations have a three-fold spreading and the ordinary dislocation do not dissociate [4]. There has been some controversy, about which fault dissociation scheme according to Eq. 2.16 or Eq. 2.15 is the correct one and hence should be applied interpret the findings. Wiezorek and Humphreys [21] suggest that Eq. 2.15 is the correct scheme supported through weak beam image simulations of different dislocation cores and comparing them with experimental data. It should be noted that here always a stoichiometric γ-TiAl is assumed in the theoretical calculations, Al-rich compositions appear in the experiments.
A special property of the APB(111) in the stoichiometric TiAl was found in the theoretical study [14, 16], namely the mechanical instability of the APB(111) with respect to the CSF. There is no local minimum on the γ-surface along the path from the APB to the CSF. This is counter-intuitive since the APB position corresponds to atom positions with just inverted occupation.

Experimental and theoretical studies have also been carried out examining alloying influence on the stacking fault energies.
Asta and Quong [23] studied the behavior of the APB(111) due to off-stoichiometry (Al-rich) and temperature effects with a mixed basis potential (MBP). They distinguished in between an equilibrated and an unequilibrated APB. The two states differ in a step function behavior for the order parameter and a constant concentration over the fault plane in the unequilibrated state, and a continuous change of the order parameter and a higher Al concentration in the vicinity of the fault than in the bulk for the equilibrated state. Starting from a value of 720 $\frac{\mathrm{mJ}}{\mathrm{m}^2}$ for stoichiometric TiAl at 0 K, the values for 54% Al at 1300 K change to 590 $\frac{\mathrm{mJ}}{\mathrm{m}^2}$ and 230 $\frac{\mathrm{mJ}}{\mathrm{m}^2}$ for unequilibrated and equilibrated state, respectively.
Woodward and Maclaren [24] studied the effect of off-stoichiometry and ternary additions on the planar fault energies using the LKKR-CPA method. They found decreasing SF values for increasing Al content in binary alloys. Starting from stoichiometric TiAl, the SISF

Table 2.1: Literature values for stacking fault energies in stoichiometric γ-TiAl, all values in $\left[\frac{\mathrm{mJ}}{\mathrm{m}^2}\right]$

Ref.	**APB(010)**	**APB(111)**	**CSF**	**SISF**	**twin**	**method**
[14]	438	667	363	172	96	LDA-FLAPW
[15]			355	184		PAW PW91-GGA (VASP)
[16]		710	314	134		FP-LMTO
[17]		499	329	137		UPP PW91-GGA (CASTEP)
[18]		663	400	170		UPP PW91-GGA (VASP)

energy drops from 123 $\frac{mJ}{m^2}$ to 98 $\frac{mJ}{m^2}$ for Ti-54Al. They proposed also decrease in the SISF for ternary additions of 2 at% Cr and 2 at% Nb keeping the Al concentration 48 at%. With increasing amount of Al (keeping Nb or Cr amount constant) the SFE increase. The SISF values for ternary additions increase in comparison to stoichiometric values for Al concentrations greater than 50 at% Al. The SISF energy predicted for the alloy Ti-48Al-2Nb is 56 $\frac{mJ}{m^2}$ and for Ti-48Al-2Cr is 70 $\frac{mJ}{m^2}$. Wen and Sun [15] predicted decreasing the SISF energy to 64 $\frac{mJ}{m^2}$ for 48.3% Al (in comparison to 184 $\frac{mJ}{m^2}$), but an increased value of 212 $\frac{mJ}{m^2}$ for increased Al concentration of 51.7% in binary alloys.
It has been reported experimentally that the tendency for deformation twinning increases with lower Al concentrations for binary single crystals [25].
The stacking fault energies in Nb-containing alloys and/or Al-poor alloys have been experimentally investigated by Zhang and Appel [26]. The SISF increases with increasing Al concentration in binary alloys, e.g. SISF of Ti-49Al is 91 $\frac{mJ}{m^2}$ while in Ti-45Al is has a value of 67 $\frac{mJ}{m^2}$. The values obtained for Nb additions are 69 $\frac{mJ}{m^2}$ for Ti-45-10Nb and 66 $\frac{mJ}{m^2}$ for Ti-49-10Nb. It should be noted that the stacking fault energies were evaluated using isotropic elasticity and that the shear modulus at 1273 K (μ=57 GPa) is used in the evaluation. In a similar study, Yuan *et al.* [27] reports values 63 $\frac{mJ}{m^2}$ for Ti-48Al-1Nb and 34 $\frac{mJ}{m^2}$ for Ti-48Al-10Nb, assuming isotropic elastic behavior with a shear modulus μ=70 GPa. A two fold dissociation was found which was assumed to correspond to the dissociation scheme given in Eq. 2.21, where only the SISF is bound by partials.

2.6 Generalized stacking fault energy

After cutting a perfect crystal across a single plane into two parts, mutually displacing them by an arbitrary vector $\vec{f}$ and rejoining the crystal, the rejoined crystal will have a surplus in energy. Normalizing this surplus energy with respect to the cross-section area gives "generalized" stacking fault energy surface, $\gamma(\vec{f})$. For an arbitrary fault vector $\vec{f}$, there

Table 2.2: Experimental values for planar fault energies in γ-TiAl, all values represented in $\left[\frac{mJ}{m^2}\right]$. [a)] Analysis of data with cubic elastic constants,[b)] data re-evaluated with tetragonal elastic constants,[c)] data attained through image shift corrections. Given temperatures are the deformation temperatures of the samples. "WB" stands for weak beam TEM. Modified table after [4].

Ref.	APB(010)	APB(111)	SISF	method	note
[9, 19]		145	77	WB[a)], 25 °C	54% Al
[9, 19, 20]	210	253	143	WB[b)], 25 °C	54% Al
[9, 21]	>250		140	WB[c)], 25 °C	54% Al
[22]			116(185[c)])	WB, 25 °C	56% Al

is a restoring stress across the cut plane [28].

$$\vec{F}(\vec{f}) = -\nabla(\gamma(\vec{f})) \tag{2.22}$$

The restoring stress is non-zero except for periodic points or for $\vec{f} = 0$ and has at least maxima in between the periodic lattice points. In different structures there exist additional metastable minimum on this surface for non-zero $\vec{f}_s$. The restoring stress at local minimum becomes zero, and a classical stacking fault or planar fault with the vector $\vec{f}_s$ can occur [28, 29].

2.7 Critical twinning shear from an ab initio criterion

Classical models predict that the critical twinning stress depends on the intrinsic stacking fault energy only. As an example the relation:

$$\tau_{\text{crit.}} \sim \frac{K\gamma_{\text{ISF}}}{|\vec{b}_{\text{twin}}|}, \tag{2.23}$$

where K is a fitting constant, is often used. The energy pathways for twinning can be discussed in the framework of the generalized planar fault energy/ generalized stacking fault energy [6, 30, 31]. In the paper of Kibey *et al.* [30] a dislocation based theory for twinning stress of fcc metals is developed. The key properties of the model are summarized below. Different dislocation based mechanisms have been proposed to explain twin nucleation in fcc materials, their common feature is the glide of Shockley partial dislocations on successive {111} planes to create multi-layered faults to then generate a twin. A three layer twin nucleus is assumed and the dislocations are treated as co-planar. Only one partial dislocation is glissile in this configuration and will cause widening of the twin nucleus [32]. A total elastic energy approach is made for the partial dislocations involved.

$$E_{\text{total}} = E_{\text{edge}} + E_{\text{screw}} - W_\tau + E_{\text{GPFE}}, \tag{2.24}$$

where E_{edge} is the energy of the edge dislocation, E_{screw} the screw dislocation energy part, W_τ the work done by applied stress τ to displace the leading partials through the width d and E_{GPFE} the generalized planar energy consideration. The edge components are treated as single pileup [33] and the screw components of the partials as finite sized vertical wall [34]. The energy E_{GPFE} is decomposed in two parts, the part of forming an intrinsic stacking fault, $E_{\gamma\text{-SF}}$, and the part of forming a twin nucleus, $E_{\gamma\text{-twin}}$. It is mentioned that $E_{\gamma\text{-SF}}$ is correlated with the energy required for cross-slip at the onset of stage III hardening. The total energy is minimized with respect to the width d and the number of the layers for the twin nucleus, N [30]. A closed form expression was found [30]:

$$\begin{aligned}\tau(d) =& \frac{G_{\{111\}}N}{\pi d}\left[\frac{|\vec{b}_s|^2}{9}+\frac{|\vec{b}_e|^2}{4(1-\nu)}\right]+\frac{2}{3N|\vec{b}_{\text{twin}}|}\left(\frac{3N}{4}-1\right)\left[\gamma_{\text{ut}}+\frac{2\gamma_{\text{tsf}}+\gamma_{\text{isf}}}{2}\right]\\ &-\frac{2}{3N|\vec{b}_{\text{twin}}|}\left(\gamma_{\text{ut}}+\gamma_{\text{isf}}\right)+\frac{1}{6|\vec{b}_{\text{twin}}|}\left[\gamma_{\text{ut}}-\frac{2\gamma_{\text{tsf}}+\gamma_{\text{isf}}}{2}\right]\\ &\left(\frac{w}{d}\right)\left[\ln\left(\frac{d+\sqrt{d^2+w^2}}{w}\right)\right]-\frac{(N-1)}{3N}\left[\gamma_{\text{ut}}-\frac{2\gamma_{\text{tsf}}}{\gamma_{\text{isf}}}\right]\\ &\left(\frac{w}{d}\right)\left[\ln\left(\frac{d+\sqrt{d^2+w^2}}{w}\right)+\frac{d}{\sqrt{d^2+w^2}}\right]\\ &+\frac{1}{3N|\vec{b}_{\text{twin}}|}\left(\gamma_{\text{us}}-\gamma_{\text{isf}}\right)\left(\frac{w}{d}\right)\left[\ln\left(\frac{d+\sqrt{d^2+w^2}}{w}\right)+\frac{d}{\sqrt{d^2+w^2}}\right]\end{aligned} \tag{2.25}$$

$\vec{b}_s$ and $\vec{b}_e$ are the screw and edge components of the Burgers vector, and $\vec{b}_{\text{twin}}$ the twinning partial of the dislocation configuration. w is the dislocation core width, and $G_{\{111\}}$ is the shear modulus of the activated $\{111\}$ plane [30]. For a cubic crystal the shear modulus is [35]:

$$G_{\{111\}} = \frac{3C_{44}\left(C_{11}-C_{12}\right)}{4C_{44}+C_{11}+C_{12}}, \tag{2.26}$$

where the C_{ij} are the components of the stiffness tensor in the Voigt's notation.
Further simplification through neglecting the first term, setting $N = 3$, and assuming $w \ll d$ leads to [15]:

$$\tau_{crit.} = \frac{5}{18b_{\text{twin}}}\left[\gamma_{\text{ut}}+\frac{2\gamma_{\text{tsf}}+\gamma_{\text{isf}}}{2}\right]-\frac{2}{9b_{\text{twin}}}\left(\gamma_{\text{us}}+\gamma_{\text{isf}}\right). \tag{2.27}$$

Therefore the critical twinning shear does not only dependent on the intrinsic stacking fault energy, but also depends on the twin boundary energy and the respective unstable energies (energy barriers) and the twinning partial length.

Chapter 3

Theoretical methods

3.1 Density Functional Theory

3.1.1 Schrödinger equation

The equation for the quantum mechanical description of the electron, was postulated by Schrödinger and states:

$$\hat{H}\phi(\vec{r},t) = i\hbar\frac{\partial}{\partial t}\phi(\vec{r},t), \tag{3.1}$$

where $\hat{H}$ is the Hamiltonian operator, $\hbar$ is the reduced Planck constant, $\vec{r}$ is the position, t the time and ϕ the wave function of the electron. The Hamiltonian operator is defined as:

$$\hat{H} = -\frac{\hbar^2}{2m}\nabla^2 + V(\vec{r},t) \tag{3.2}$$

The first term is the kinetic energy of the electron and $V(\vec{r},t)$ describes the potential in which the electron "lives". The time independent equation is:

$$\hat{H}\psi(\vec{r}) = E\psi(\vec{r}) \tag{3.3}$$

E is the energy of the state (the energy eigenvalue of the state). Multiplying the wave function with its complex conjugate is interpreted as the probability density of finding the electron/particle at a given location, and not the charge or mass distribution [36].

3.1.2 Formulation of a many-body problem

For more than one particle, the eigenvalue equation, Eq. 3.3, changes to:

$$\hat{H}\psi(\vec{r}_i,\vec{R}_i,t) = E\psi(\vec{r}_i,\vec{R}_i,t), \tag{3.4}$$

where $\vec{r}_i$ and $\vec{R}_i$ are coordinates of the electrons and nuclei [37].

A solid can be viewed as a collection of positively charged ions at positions $\vec{R}_i$, and much lighter electrons at positions $\vec{r}_i$. Let Z be the atomic number (assuming all atoms are the same) and N be the number of atoms. The problem translates into solving a system of $N + ZN$ mutually interacting objects. This is called a many-body problem. The exact Hamiltonian considering only electrostatic interactions between particles is:

$$\hat{H} = -\frac{\hbar^2}{2}\sum_i \frac{\nabla^2_{\vec{R}_i}}{M_n} - \frac{\hbar^2}{2}\sum_i \frac{\nabla^2_{\vec{r}_i}}{m_e} - \frac{1}{4\pi\epsilon_0}\sum_{i,j}\frac{e^2 Z}{|\vec{R}_i - \vec{r}_j|} + \frac{1}{8\pi\epsilon_0}\sum_{i\neq j}\frac{e^2}{|\vec{r}_i - \vec{r}_j|} + \frac{1}{8\pi\epsilon_0}\sum_{i\neq j}\frac{e^2 Z^2}{|\vec{R}_i - \vec{R}_j|} \,. \tag{3.5}$$

The first term is the kinetic energy of the nuclei, the second term is the kin. energy of the electrons, the third one is the Coulomb interaction between the nuclei and electrons. The fourth term is the electron-electron Coulomb interaction and the last one is the nuclei-nuclei interaction. For practical applications, it is impossible to solve such an equation without further approximations.
Compared to electrons, nuclei are several orders of magnitude heavier (mass of an electron $m_e = 9.1 \times 10^{-31}\,\mathrm{kg}$ vs. mass of a proton $m_p = 1.7 \times 10^{-27}\,\mathrm{kg}$). For a given constant momentum this means that a nucleus moves much slower than an electron. Therefore, nuclei can be taken as static, and only the electronic part of the wave function remains to be solved. The nuclei interact with the electrons through a static positive background potential. This approximation is known as the Born-Oppenheimer approximation.

Under this approximation the kinetic energy of the nuclei is zero, and the nucleus-nucleus interaction reduces to a constant. In Eq. 3.5, only kinetic energy of the electrons, $\hat{T}$, the electron-electron potential energy, $\hat{V}$, and the electron-nucleus interaction which can be interpreted as an external potential, $\hat{V}_{\mathrm{ext}}$, remain. So the Hamiltonian becomes [38, 39]:

$$\hat{H} = \hat{T} + \hat{V} + \hat{V}_{\mathrm{ext}} \,. \tag{3.6}$$

3.1.3 Theorems of Hohenberg, Kohn and Sham

Today several different ways exist to further simplify the Schrödinger equation to be solved. A modern method for solid state calculations is the Density Functional Theory (DFT) [40]. DFT works with the electron density, $\rho(\vec{r})$, as the main variable, hence replacing the many-body wave-function.
The central ideas of DFT were formulated in several theorems. The first theorem states

> Theorem 1: There is a one-to-one correspondence between the ground state density $\rho(\vec{r})$ of a many-electron system and the external potential $\hat{V}_{\mathrm{ext}}$ (up to an additive constant).

The electron charge density $\rho(\vec{r})$ can be calculated from the many-electron wave function as

$$\rho(\vec{r}) = \sum_{i=1}^{N} \int \Psi^*(\vec{r}_1, \vec{r}_2, \ldots, \vec{r}_i \equiv \vec{r}, \ldots, \vec{r}_N) \cdot \Psi(\vec{r}_1, \vec{r}_2, \ldots, \vec{r}_i \equiv \vec{r}, \ldots, \vec{r}_N) d\vec{r}_1 d\vec{r}_2 \ldots d\vec{r}_N \ . \tag{3.7}$$

For an external potential $\hat{V}_{\text{ext}}$ $\rho(\vec{r})$ is fully determined through the many-electron wave function Ψ. However, the consequence of the first theorem of Kohn & Hohenberg is that the electron density has the same amount of information contained as the many-electron wave function in terms of what knowledge can be extracted about atoms and material behavior.

THEOREM 2: For the Hamiltonian $\hat{H}$ (Eq. 3.6), the ground state total energy functional $H[\rho] = E_{V_{\text{ext}}}[\rho]$ is of the form

$$\begin{aligned} E_{V_{\text{ext}}}[\rho] = & \underbrace{\langle \Psi | \hat{T} + \hat{V} | \Psi \rangle}_{F_{HK}[\rho]} + \langle \Psi | \hat{V}_{\text{ext}} | \Psi \rangle \\ = & \ F_{HK}[\rho] + \int \rho(\vec{r}) V_{\text{ext}}(\vec{r}) d^3\vec{r} \end{aligned} \tag{3.8}$$

where the Hohenberg-Kohn density functional $F_{HK}[\rho]$ is universal for any many-electron system. $E_{V_{\text{ext}}}[\rho]$ reaches its minimal value (equal to the ground state total energy) for the ground state density corresponding to V_{ext} [38, 39].

Consequently, it is possible to use variational principle to find the ground state electron density which minimizes $E_{V_{\text{ext}}}[\rho]$. The HK-functional can be further split up into:

$$F_{HK}[\rho] = T_0[\rho] + V_H[\rho] + V_{xc}[\rho]. \tag{3.9}$$

$T_0[\rho]$ is the kinetic energy of fictitious non-interacting electron gas, V_H is the Hartree and V_{xc} is the exchange-correlation potential.

THEOREM 3: The exact ground state electron density $\rho(\vec{r})$ of an N-electron system is

$$\rho(\vec{r}) = \sum_{i=1}^{N} \phi_i^*(\vec{r}) \phi_i(\vec{r}) \tag{3.10}$$

where the single-particle wave functions $\phi(\vec{r})$ are the N-lowest energy solutions of the Kohn-Sham equation

$$\hat{H}_{KS} \phi = \epsilon \phi \tag{3.11}$$

where

$$\hat{H}_{KS} = \underbrace{-\frac{\hbar^2}{2m_e} \nabla^2}_{\hat{T}_0} + \underbrace{\frac{e^2}{4\pi\epsilon_0} \int \frac{\rho(\vec{r}')}{|\vec{r}' - \vec{r}|} d^3\vec{r}'}_{\hat{V}_H} + \hat{V}_{xc} + \hat{V}_{\text{ext}} \ . \tag{3.12}$$

The single particle wave functions do have only a meaning in terms of the electron density, alone they are i a way artificial. A important note is that the Hartree potential , V_H, and the exchange-correlation potential, V_{xc}, depend on the electron density ρ itself. Hence the problem is solved by an iterative procedure, where the initial electron density $\rho_0(\vec{r})$ is guessed to construct the potentials and to solve the Kohn-Sham equation after which a new electron density $\rho_n(\vec{r})$ is constructed from the solution. This scheme is repeated until self-consistency is reached.
In summary, solving many coupled partial differential equations corresponding to a many-body Schrödinger equation is transformed to solving a Schrödinger-like equation of non-interacting particles in the framework of the Kohn-Sham theory, or the Density Functional Theory. It gives the possibility to solve systems with sizes of around hundred to thousand particles [38, 39]

3.1.4 The exchange-correlation potential

The exact form of the exchange-correlation potential, V_{xc}, is unknown and needs to be approximated. A widely used form is the local density approximation (LDA) proposed by Kohn and Sham [41]:

$$V_{xc}^{\mathrm{LDA}}[\rho] = \int \rho(\vec{r})\epsilon_{xc}(\rho(\vec{r}))\ d^3\vec{r}. \tag{3.13}$$

The function ϵ_{xc} is the density of the exchange-correlation energy derived for a homogeneous electron gas (jellium model). The exchange-correlation energy density depends on the value of electron density at a particular point $\vec{r}$ only. Another approach is the generalized gradient approximation (GGA) which depends on the electron density and it's gradient:

$$V_{xc}^{\mathrm{GGA}}[\rho] = \int \rho(\vec{r})\epsilon_{xc}(\rho(\vec{r}), |\nabla\rho(\vec{r})|)\ d^3\vec{r}\ . \tag{3.14}$$

There exist different forms for the functional ϵ_{xc} optimized to best fit various properties of a large set of experimental data. The often used parametrization is the one of Perdew, Burke, and Ernzerhof [42] usually termed as PBE.

3.1.5 The VASP code

The *ab initio* calculations in this thesis are all carried out with the Vienna Ab initio Simulation Package (VASP).
"VASP is a complex package for performing *ab initio* quantum-mechanical molecular dynamics (MD) simulations using pseudo potentials or the projector-augmented wave (PAW) method and a plane wave basis set. The approach implemented in VASP is based on the (finite-temperature) local-density approximation with the free energy as variational quantity and an exact evaluation of the instantaneous electronic ground state at each MD time step." [43, 44]

3.2 Molecular Dynamics

Molecular Dynamics (MD) treats the atoms as classical particles, i.e. the system's evolution is described by Newton's equations of motion. The interatomic potentials to describe the behavior of the atoms are fitted to empirical data. Once the starting positions and the velocities are given, the time-evolution of the atoms can be straightforwardly modeled.
If $\vec{F}$ is the sum of all forces acting on an atom, the corresponding equation of motion reads

$$\vec{F} = m\vec{a} = m\frac{\mathrm{d}\vec{v}}{\mathrm{d}t} = m\frac{\mathrm{d}^2\vec{r}}{\mathrm{d}t^2} = \frac{\mathrm{d}\vec{p}}{\mathrm{d}t} \tag{3.15}$$

where $\vec{a}$ is the acceleration, $\vec{v}$ is the velocity, $\vec{r}$ is the position, and $\vec{p}$ the momentum of the atom. For an isolated system, $\vec{F}$ is:

$$\vec{F} = -\nabla U \tag{3.16}$$

the gradient of the potential, which is a function of interatomic distances. [37]

Potentials for specific systems are created by fitting certain functions to experimental data or calculated data from *ab initio* methods. Out of many different potentials available today, in this study the embedded atom method potentials are applied.
The embedded atom method takes the effective electron density at a given atomic site as one of it's parameters. Therefore, some electronic effects can be captured. The embedding energy describes energy required to embed positively charged atom cores into the electron cloud. The potentials are of the form

$$U_{\mathrm{EAM}} = \sum_{i \neq j} U_{ij}(r_{ij}) + \sum_{i} F_i(\rho_i) \tag{3.17}$$

where $F_i(\rho_i)$ is the embedding energy function, and the r_{ij} the distance between the ith and the jth atom. The electron density ρ_i is a linear superposition of the electron clouds from all other atoms

$$\rho_i = 1/2 \sum_{j(\neq i)} \rho_j(r_{ij}) \tag{3.18}$$

For alloys, the fitting of the embedding functions for constituting elements is difficult, so there is only a limited number of potentials available [37].

3.3 The LAMMPS code

"LAMMPS is a classical molecular dynamics code that models an ensemble of particles in a liquid, solid, or gaseous state. It can model atomic, polymeric, biological, metallic, granular, and coarse-grained systems using a variety of force fields and boundary conditions." [45]

The acronym LAMMPS stands for Large-scale Atomic/Molecular Massively Parallel Simulator. It is especially capable of using EAM potentials and has freely available potentials for a large variety of elements [46].

3.4 Visualization

All images of atomic arrangements in this thesis were built with the VESTA 3 [47].

Chapter 4

Results

4.1 Calculation settings

If not mentioned otherwise the same settings for the self consistent solver are applied for all of calculations. The k-point mesh was chosen to be automatically generated with the built-in method of the Monkhorst-Pack scheme using a "length" input parameter 70. The KPOINT file of VASP looks like as followed:

```
k-points
0
A
70
```

The cut-off energy for the plane wave basis set is set to 400 eV, and the convergence criterion for the electronic loop was set to 10^{-7} eV in the total energy. As TiAl is a non-magnetic system, spin polarization was not included in our calculations. For the ionic relaxation, if applied, the forces were relaxed to 3×10^{-2} eV/Å. A representative example of the INCAR file which is used with this settings is given below:

```
Ti-Al gamma
ENCUT = 400
PREC = accurate
ALGO = Fast
EDIFF = 1E-07
ISPIN = 1
NSW = 100
IBRION = 2
EDIFFG = -3E-02
```

```
ISIF = 2
LREAL = T
LCHARG = False
LWAVE = False
```

The used potential for the Ti atoms is the "PAW_GGA Ti_sv 07Sep2000", and the "PAW_GGA Al 05Jan2001" for the Al atoms.
The standard lattice constants in this thesis were defined to be a=3.9675 Å, and c=4.0489 Å.

4.2 Build up of the planar fault geometries

4.2.1 The layer model

In contrast to the conventional unit cell representation of the $L1_0$ structure as shown in Fig. 2.1, the same structure can be also be seen as a stacking of (111) planes "ABC..."(see Sec. 2.3.2). The planar unit cell generating the (111) planes contains 2 atoms, one Al and one Ti. The supercell $\vec{a}$ and supercell $\vec{b}$ direction are chosen to be $\vec{a} = 1/2[11\bar{2}]$ and $\vec{b} = 1/2[\bar{1}10]$, the coordinates of the first atom (Al) are [000] the second occupies the position $\frac{\vec{a}+\vec{b}}{2}$. Let $\vec{v}$ be the direction $\vec{v} = 1/3[111]$ and $\vec{b}_3 = 1/6[11\bar{2}]$. Then the second layer starts with the position of the first layer Al atom $\overrightarrow{\mathrm{Al}_0} = [000]$ shifted by $\vec{v}$ and $\vec{b}_3$, $\overrightarrow{\mathrm{Al}_1} = \overrightarrow{\mathrm{Al}_0} + \vec{b}_3 + \vec{v}$. The second Ti atom sits at $\overrightarrow{\mathrm{Ti}_1} = \overrightarrow{\mathrm{Al}_1} + \vec{a}/2 + \vec{b}/2$. The layers "AB" are now built, the "C" layer follows the same scheme: the position of the second Al atom is shifted by $\vec{v}$ and $\vec{b}_3$, and $\overrightarrow{\mathrm{Ti}_i} = \overrightarrow{\mathrm{Al}_i} + \vec{a}/2 + \vec{b}/2$. The fourth layer position is defined by the position of the first layer Al atoms $\overrightarrow{\mathrm{Al}_0}$ shifted by [111], and the procedure of building the two following "BC" layers is repeated again. The supercell lattice vector of an n-layer cell of γ-TiAl is $\vec{c} = n/3[111]$. To preserve the crystal symmetry, n must be a multiple of three. The scheme is shown in Fig. 4.1.

Due to the application of periodic boundary conditions (PBC) by the VASP code calculations, there are different approaches to build the stacking fault supercell structures. Two different methods to generate the stacking fault "geometries" are applied in this thesis. They are discussed in the following subsections 4.2.2 and 4.2.3.

4.2.2 Displacement geometries

This approach uses the supercell after the procedure described in Sec. 4.2.1. The the number of (111) planes is adjusted to ensure that the sequence is not violated through the PBC, and the upper part of the crystal gets translated through a fault vector which creates the fault in the supercell. The atoms in the fault part of the crystal are translated by the fault vector $\vec{b}_i$ to their new position. The supercell lattice vectors stay the same as in the layer model of

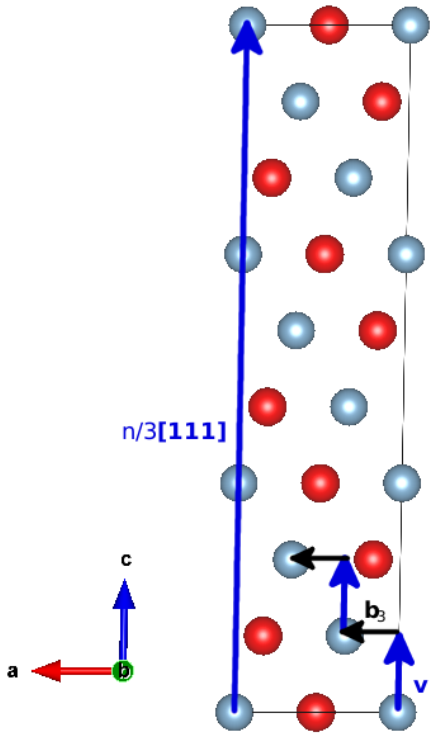

Figure 4.1: Build-up of the $L1_0$ structure with the layer model in the $\vec{b} = 1/2[\bar{1}10]$ projection, $\vec{v} = 1/3[111]$, $\vec{b}_3 = 1/6[11\bar{2}]$.

the $L1_0$ structure. If the absolute position of the shifted atom is not inside supercell, VASP automatically maps it back into the cell through the PBC. The SISF, SESF, CSF, APB(111) and the twin boundary have been implemented this way.

SISF

The supercell can be build so that it contains only one stacking fault in the supercell geometry. For that, the total number of layers must fulfill $n = 5 + 3m$ to maintain the correct sequence, where m is a positive integer (see Fig. 4.2). The correct sequence here means that the last layer in this model a, "C" layer, is followed along the supercell $\vec{c}$ direction by an "A" layer through the periodic image of the first layer. This constraint causes that the total number of layers, n, is not a multiple of three any more.

SESF

The superlattice extrinsic stacking fault can also be build containing only one stacking fault per supercell. The relation $n = 7 + 3m$ has to be fulfilled for the correct sequence. The fault is shown in Fig. 4.3.

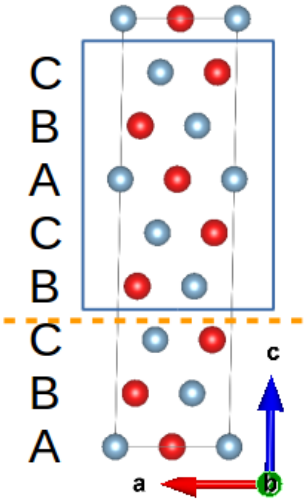

Figure 4.2: A SISF supercell, the dashed line indicates the position of the stacking fault. Atoms enclosed in a blue rectangular are shifted by the $\vec{b}_3$ vector from their ideal positions to create the SF. Supercell directions as described in Sec. 4.2.1.

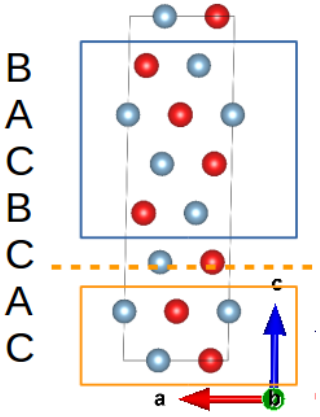

Figure 4.3: A SESF supercell, dashed line is at the position of the fault layer. Atoms enclosed in a blue rectangular are translated by the fault vector $\vec{b}_3$, atoms enclosed in an orange rectangular are translated by $-\vec{b}_3$ from their ideal positions.

CSF

For the complex stacking fault it is not possible to build a supercell containing only one stacking fault. Again, starting from a supercell from perfect γ-TiAl the positions are translated the way shown in Fig. 4.4. It should be noted that in this model the fault-fault spacing is different for the primed and unprimed region.

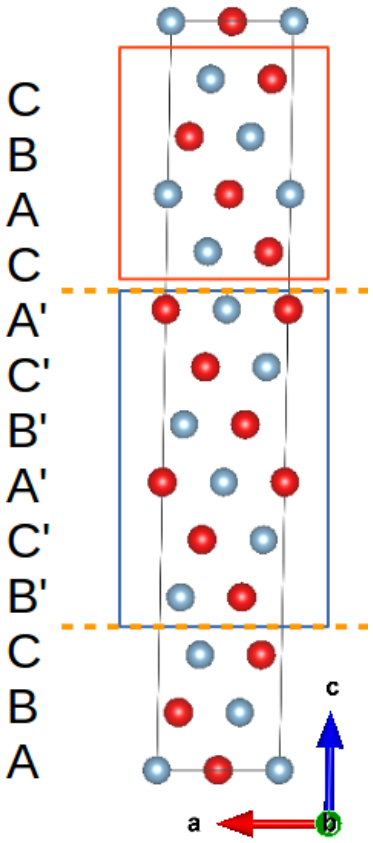

Figure 4.4: A CSF supercell. The dashed lines illustrate the complex stacking faults. Blue enclosed atoms are displaced by a vector of $\vec{b}_1 = 1/6[\bar{2}11]$ from their ideal positions, the red line enclosed atoms are displaced by the vector of $-2\vec{b}_1$ from their ideal $L1_0$ position. Primed letters indicate reversed occupation in the cell, i.e., Al atoms on Ti positions and vice versa.

APB

A similar situation arises also for the APB, where two faults have to be present in the supercell, and inverted occupation appears. The exact geometry is discussed in the Fig. 4.5. The total number of layers, n, is a multiple of three; to maintain equal spacing between the faults, n should be chosen as $n = 12 + 2m$.

Twin

It is more intuitive that two boundaries exist in the supercell in the case of the twin geometry. To build the true twin geometry as described in Sec. 2.4.3 the layers above a chosen twin boundary are translated by $o\vec{b}_3$, where o denotes the number of layer distances from the twin boundary (which becomes the mirror plane). The geometry of the model is shown in Fig. 4.6.

The fault-fault spacing is chosen to be the same for both twin variants.

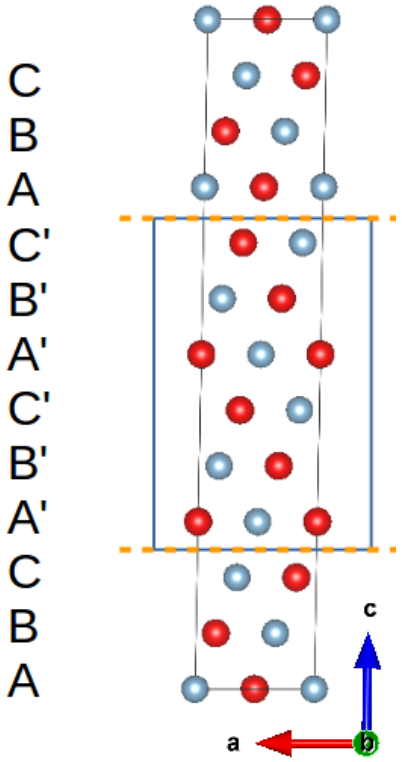

Figure 4.5: An APB supercell, dashed lines show the actual APB position. Primed letter indicate the inverted occupation of the lattice.

4.2.3 Pseudo-shear approach

A starting point for this build up of the fault geometries is again the supercell as described in Sec. 4.2.1. In contrast to the previous approach the absolute coordinates of the atoms do not change. The fault is produced by the application of PBC and tilting the supercell $\vec{c}$ lattice vector. In a perfect supercell, $\vec{c} = n/3[111]$, while the $\vec{c}$ direction is tilted by the fault producing vector $\vec{b}_i$. Hence, the changed supercell direction $\vec{c}$ fulfills the condition $\vec{c} = \vec{b}_i + n/3[111]$. The supercell $\vec{a}$ and supercell $\vec{b}$ lattice vectors remain unchanged. In this way, it is always possible to build a supercell containing only one fault layer per supercell. The application is demonstrated in Fig. 4.7 for an APB(111). In this approach $n = 3m$ is used to have perfect $L1_0$ structure between the fault layers.
The APB(010) is built in a similar manner the difference being that conventional unit cells are stacked along the [010] direction (which is tilted by the distinct fault vector) instead of stacking (111) planes.

This approach is additionally suitable to calculate GSFE in a straight forward way. The fault vectors $\vec{b}_i$ are replaced by arbitrary vectors of the "generalized" fault $\vec{t}$, so $\vec{c} = \vec{t} + n/3[111]$. The fault vector is $\vec{t} = u/2[11\bar{2}] + w/2[\bar{1}10]$, where u and w are in the range of [0...1].

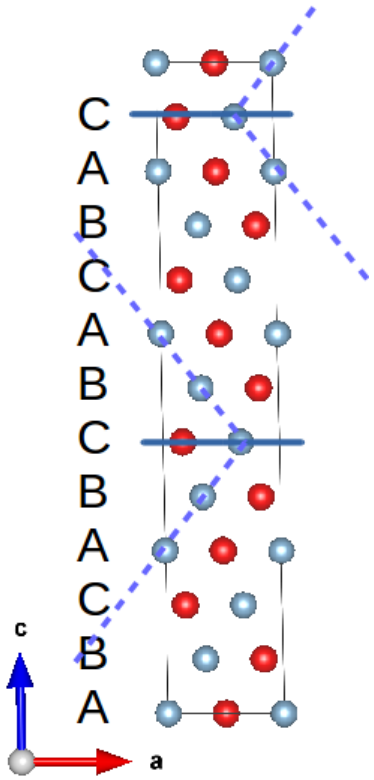

Figure 4.6: A supercell containing twin boundaries. Blue dashed lines are eye guides for a better interpretation of the structure. Blue solid lines indicate the coherent twin boundaries. The supercell is shown along the $-\vec{b}$ direction.

4.3 Results for the planar faults

The total energy for the conventional cell and the supercell for the perfect γ-TiAl were calculated with the lattice constants given in Sec. 4.1. The energy per two atoms is equal for both cases within the numerical accuracy.
The evaluation of the stacking fault energies for supercells containing one stacking fault is done via:

$$\gamma = \frac{E - E_0}{A} \tag{4.1}$$

where γ is the stacking fault energy, E is the total energy of the supercell with the fault, E_0 the energy of the perfect crystal with the same number of layers and A is the cross-section area of the fault in one cell. For the (111) stacking faults:

$$A = |\vec{a} \times \vec{b}| \tag{4.2}$$

is used to calculate the cross-section area, when $\vec{a}$ and $\vec{b}$ are the supercell lattice vectors. For faulted supercells, where a perfect crystal can not be build due to the reason that the number of layers n is not a multiple of three in the fault containing cell, and/or the number

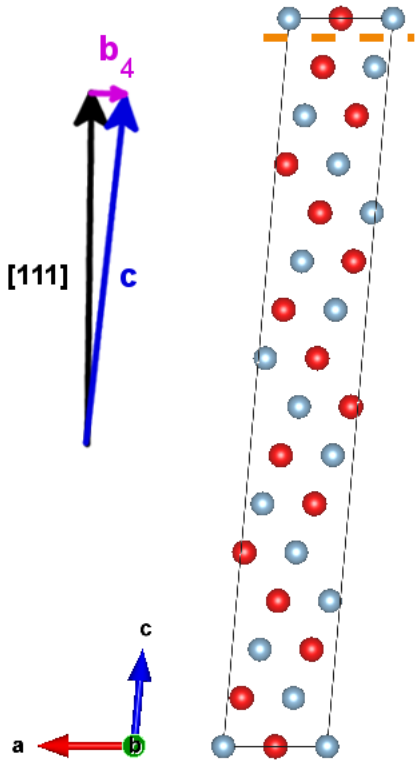

Figure 4.7: APB(111) with $n = 15$ layers implemented, dashed orange line indicates the fault plane. Differences in the supercell $\vec{c}$ directions are drawn additionally. $\vec{b}_4 = 1/2[01\bar{1}]$

of faults in the supercell is larger than one, a modified formula is used:

$$\gamma = \frac{E - nE_{\text{perlayer}}}{NA}. \tag{4.3}$$

E_{perlayer} is the energy per (111) layer in the perfect crystal model and N is the number of faults in 1 supercell. For a large enough n, Eqs. 4.1 and 4.3 converge to a constant defining the particular stacking fault energy/planar fault energy.
The results for the calculated stacking fault energies are summarized in Tab. 4.1 for the build-up of the cells as discussed in Sec. 4.2.2, and for the scheme of Sec. 4.2.3 in Tab. 4.2. During the calculation, all the atoms were allowed to relax along the supercell $\vec{c}$ direction except for the the calculation of the APB(010) where they have been allowed to relax along the supercell $\vec{b}$ direction. It should be noted that the cross-sectional area A is different for the APB(010) than for the other faults. For a more detailed discussion of the influence of a particular relaxation scheme, the reader is referred to Sec. 4.4.1.

Table 4.1: Results for stacking fault energies with the "displacement geometries" approach as described in Sec. 4.2.2. All values are rounded and in $[\frac{\mathrm{mJ}}{\mathrm{m}^2}]$, except for n and N which denote the number of layers in the used model and the number of faults per supercell respectively. Results marked with $^{*)}$ are obtained with an energy convergence criterion for the ionic relaxation in contradiction to the force criterion applied by default (Sec. 4.1).

n	N	**APB**	**CSF**	**SISF**	**SESF**	**twin**
13	2		417			
19	2		415			
31	2		414			
14	1			188		
17	1			188		
18	2	711				
24	2	711				
$^{*)}$12	2	704				
$^{*)}$7	1				191	
$^{*)}$10	1				188	
$^{*)}$13	1				189	
$^{*)}$8	1			187		
$^{*)}$11	1			187		
12	2					115

Table 4.2: Results for stacking fault energies with the "pseudo-shear" approach 4.2.3. All values are rounded and in $[\frac{\mathrm{mJ}}{\mathrm{m}^2}]$, except for n which denotes the number of layers in the applied model (or numbers of conventional cells for the APB(010)).

n	**APB**	**CSF**	**SISF**	**APB(010)**
6		416		
15	717	415	188	
7				340

Generally, it is observed that[1]:

$$APB > CSF > SISF \tag{4.4}$$

$$SISF \sim SESF \tag{4.5}$$

$$APB(111) > APB(010) \tag{4.6}$$

4.3.1 LDA vs. GGA

To estimate the impact of different exchange-correlation potentials also the local density approximation (LDA) has been used to calculate the SFE. Specifically the "PAW Ti_sv 07Sep2000" and the "PAW Al 17Apr2000" potentials were used for Ti and Al atoms, respectively. The results are summarized in Tab. 4.3. The build-up from Sec. 4.2.3 was used with $n = 15$.

The ordering of the stacking fault energies stays the same only their absolute values are lowered for the LDA.

4.3.2 Effect of volume change

The effect of the changing cell volume was investigated for relative changes of $\pm 5\%$. The results are shown in Fig. 4.8. The supercells with increased/decreased volume were optimized with respect to the cell shape, yielding to corresponding lattice parameters. These were further used to build supercells with SF as described in Sec. 4.2.3. The SFEs were evaluated for with different cross-sectional area and E_{perlayer}, e.g. $A_{+0.05} \neq A_{-0.05} \neq A_{\text{standard}}$ so that this change has to be considered in the post-processing.

The SFEs decrease and increase with expanding and shrinking of the cell, respectively. The overall change for SISF is negligible for the studied cases though, the differences are about $\sim 2\frac{\text{mJ}}{\text{m}^2}$. This can be used to as a rough prediction for the temperature effects on SFEs: they decrease with raising temperature. It should be noted, however, that temperature effects are usually more complex as, e.g. phonons and other interactions take place.

[1]For the sake of simplicity, APB refers both to the fault as well as its energy γ_{APB}. The same applies to other abbreviations.

Table 4.3: A comparison of LDA and GGA-based stacking fault energies. Values presented in $\left[\frac{\text{mJ}}{\text{m}^2}\right]$

SF	LDA	GGA
APB	694	717
CSF	392	415
SISF	179	188

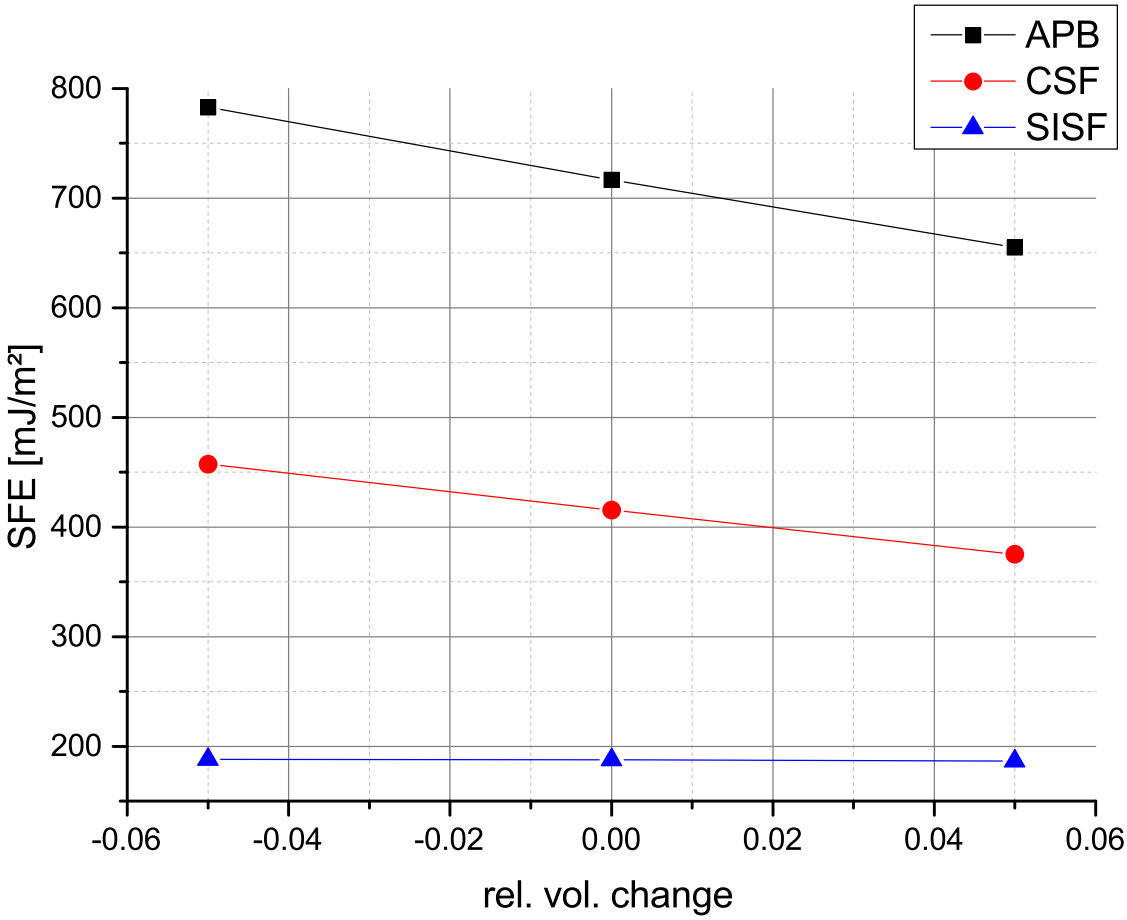

Figure 4.8: Stacking fault energies for different cell volumes.

4.3.3 Equilibrium lattice constants

The conventional unit cell of the $L1_0$ structure (as shown in Fig. 2.1) is used to determine the equilibrium lattice constants. There are four atoms in the conventional unit cell, two Al atoms at the position [000] and 1/2[110], two Ti atoms at 1/2[101] and 1/2[011]. The c/a ratio is hold constant $c/a = 1.0195$ and the a lattice constant is varied between $a = 3.9\,\text{Å}$ to $a = 4.05\,\text{Å}$. For every fixed volume, a cell shape relaxation is allowed. The energies are fitted to the Murnaghan equation of state [48] (EoS), Eq. 4.7, and the Birch-Murnaghan EoS [49], Eq. 4.8.

$$E(V) = E_0 + \frac{B_0 V}{B_{0,p}} \left(\frac{\frac{V_0}{V}^{B_{0,p}}}{B_{0,p} - 1} + 1 \right) - \frac{B_0 V_0}{B_{0,p} - 1} \tag{4.7}$$

$$E(V) = E_0 + \frac{9 V_0 B_0}{16} \left\{ \left[\left(\frac{V_0}{V} \right)^{\frac{2}{3}} - 1 \right]^3 B_{0,p} + \left[\left(\frac{V_0}{V} \right)^{\frac{2}{3}} - 1 \right]^2 \left[6 - 4 \left(\frac{V_0}{V} \right)^{\frac{2}{3}} \right] \right\} \tag{4.8}$$

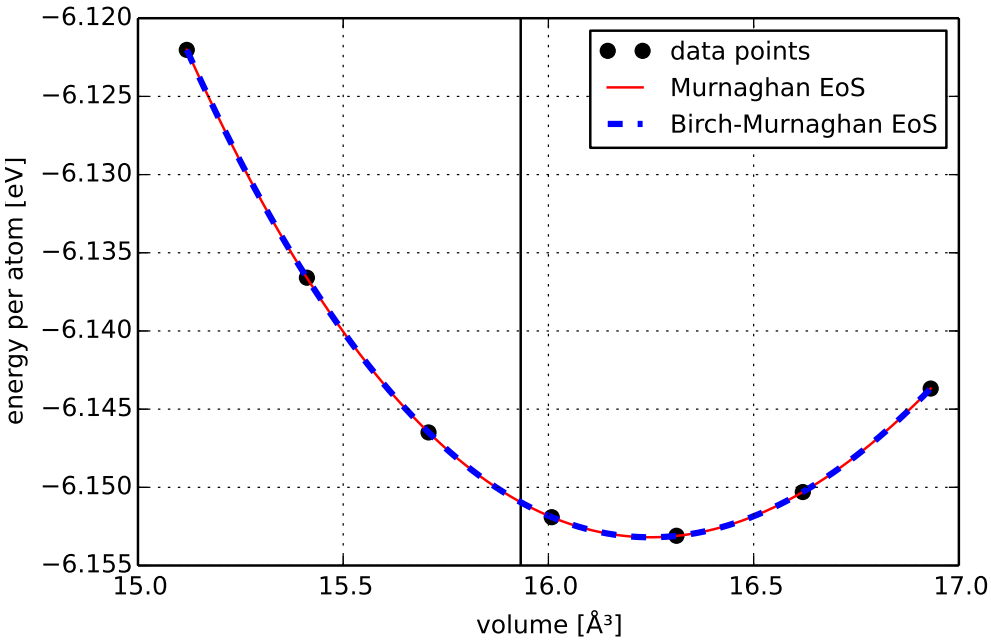

Figure 4.9: Fitted curves of observed data points to EoS. Vertical line indicates position of volume throughout this thesis as "standard" (Sec. 4.1)

B_0 is the bulk modulus, and $B_{0,p}$ is the bulk modulus derivative with respect to the pressure at $p = 0$. $E(V)$ denotes the energy as a function of the volume. E_0 and V_0 are the equilibrium energy and the equilibrium volume respectively. The data points were fitted to the EoS through the Levenberg-Marquardt algorithm implemented within the SciPy environment [50]. The fitting curves are shown in Fig. 4.9. The thus obtained parameters are summarized in Tab. 4.4.

The equilibrium volume has been used to determine the equilibrium lattice constants through a calculation where the cell was allowed to change its cell shape with given, fitted, volume, yielding lattice constants to be a=3.9915 Å and c=4.0793 Å. The so obtained energy per atom was $E_0 = -6.15321$. The agreement between the two different methods is good, only the $B_{0,p}$ differs slightly.
The equilibrium volume is about 2 % bigger than the as standard used lattice constants in this thesis. Using a linear interpolation, the stacking fault energies for the equilibrium lattice

Table 4.4: Fitted equilibrium parameters.

method	V_0 [Å^3]	B_0 [GPa]	$B_{0,p}$ [1]	E_0 [eV/atom]
Murnaghan	16.2485	113.3	3.7668	-6.15319
Birch-Murnaghan	16.2482	113.4	3.8245	-6.15319

constants can be gained from Fig. 4.8. For the APB, CSF and SISF, the energies change to 692, 400 and 187 $[\frac{\mathrm{mJ}}{\mathrm{m}^2}]$, respectively.

4.4 Generalized stacking fault energy

The (111) plane

The GSFE as described in Sec. 2.6 was calculated with the scheme discussed in Sec. 4.2.3. The resulting contour plot is represented in Fig. 4.10. The atoms were allowed to move along the [111] direction and a model with $n = 15$ layers was used. The GSFE was mapped with equidistant points with 5 points along the supercell $\vec{b}$ direction and 11 points along the supercell $\vec{a}$ direction. Data in between the grid points were interpolated. It is used as an overview and more detailed mapping is discussed in the following sections.

As can be seen from Figs 4.10 and 4.13 only in the case of APB a grid point is mapped exactly at the corresponding hard-sphere position. The minimum for the other two faults are easily seen on the plot. Finally, the energy barriers are smaller in the direction $\vec{b}$ than in the $\vec{a}$ direction.

4.4.1 Influence of the relaxation

Relaxation direction

VASP has the capability to choose the relaxation direction along any of the supercell directions [44], maximum the three supercell directions. This is usually sufficient since all directions can be chosen this way to relax the structure, only the coordinates have to be transformed. However, when using the methodology from Sec. 4.2.3 to build supercells with stacking faults, it is not any more possible to specify the "correct" direction. By the correct direction here is meant the [111] direction along which the atoms are allowed to move during the relaxation, but since the supercell $\vec{c}$ direction is always differs from $n/3$[111] by the fault producing vector $\vec{f}$, the relaxation direction is always wrong. For large enough n, though, the error gets smaller, since the fault vector stays constant, but the $n/3$[111] increases with n.

To overcome this disadvantage a modified version of the VASP code [52] was used partly in the thesis. In this modified code the relaxation direction can be selected as one of the global Cartesian coordinate system, i.e. the global z-direction was chosen as the relaxation direction for the calculations with the set up from Sec. 4.2.3. Therefore adjustments in the build-up of the cells were needed: The [111] direction needs to be rotated into the global z-axis. The rotation of the supercell is executed with the rotation point as the origin [000]

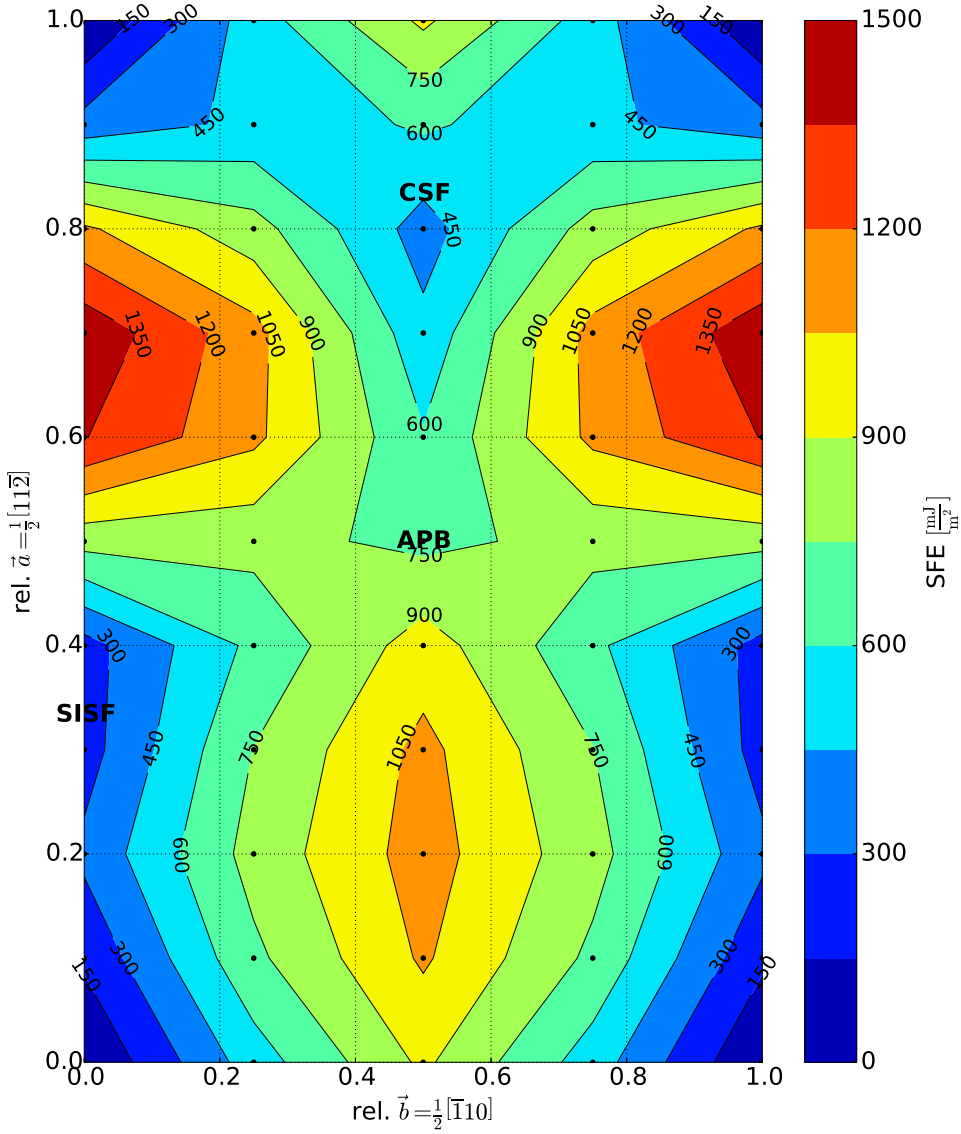

Figure 4.10: Contour plot of the GSFE for the (111) plane of stoichiometric γ-TiAl. Dots represent calculated data (grid points). SISF, APB and CSF are labeled at their position on the γ-surface. Plot was created with [51].

of the coordinate system and direction vector $\vec{a}$ which fulfills

$$\vec{a} = k\,(\vec{g} \times \vec{z}_{\text{global}}) \tag{4.9}$$

where k is a constant, $\vec{g}$ is the [111] direction and z_{global} is the global z-direction. The directions $\vec{c}$ and z_{global} are tilted away by an angle ϕ:

$$\phi = \arccos\left(\frac{\vec{g} \cdot \vec{z}_{\text{global}}}{|\vec{g}||\vec{z}_{\text{global}}|}\right). \tag{4.10}$$

The rotated coordinates of an individual atom $\vec{d}$ is then calculated from the global positions before $\vec{x}$ as [53]:

$$\vec{d}\,(\vec{x}) = (\cos\phi)\,\vec{x} + (1 - \cos\phi)\,\frac{\vec{x} \cdot \vec{a}}{|\vec{a}|^2}\vec{a} + \frac{\sin\phi}{|\vec{a}|}\vec{a} \times \vec{x}. \tag{4.11}$$

To get an overview for the error introduced through different relaxation directions, two figures are shown, one a cut through the GSFE of the (010) plane along the path to the APB(010) (Fig. 4.11), and the GSFE cut along the path to the APB(111) (Fig. 4.12). Red points are calculated using the supercell $\vec{c}$ direction as the relaxation direction, black dots are gained through relaxing along the [111] direction for $n = 15$ for the (111) fault and $n = 7$ for the APB(010).

The two different types of points are in good agreement with another forming a single curve. For direct comparison, the APB(111) calculated with both relaxation methods is represented in Tab. 4.5.

Comparing the two graphs yields that the energy barrier along the straight way from the perfect crystal to the particular fault, is bigger for the APB(010) than for the APB(111). This is an interesting observation as together with Tabs 4.1 and 4.2 points out that a smaller barrier has to be overcome to produce energetically more expensive fault. It should be also noted that for the APB(111) other paths exist where the barriers are even smaller than the straight line in Fig. 4.4.3, while for the APB(010), the straight line is very close to the minimum energy pathway.
One expects larger errors in the values for larger fault vectors $\vec{f}$ with the supercell $\vec{c}$ as relaxation direction, so mapping over a mirror plane of the crystal when calculating the GSFE would result in slightly non-symmetric values. For the other discussed relaxation direction this should not be the case, which is actually seen in 4.13 where the green and cyan lines overlap perfectly.

Table 4.5: APB(111) in $\left[\frac{\text{mJ}}{\text{m}^2}\right]$ for different relaxation directions.

relaxation direction	**APB(111)**
supercell $\vec{c}$	717
[111]	712

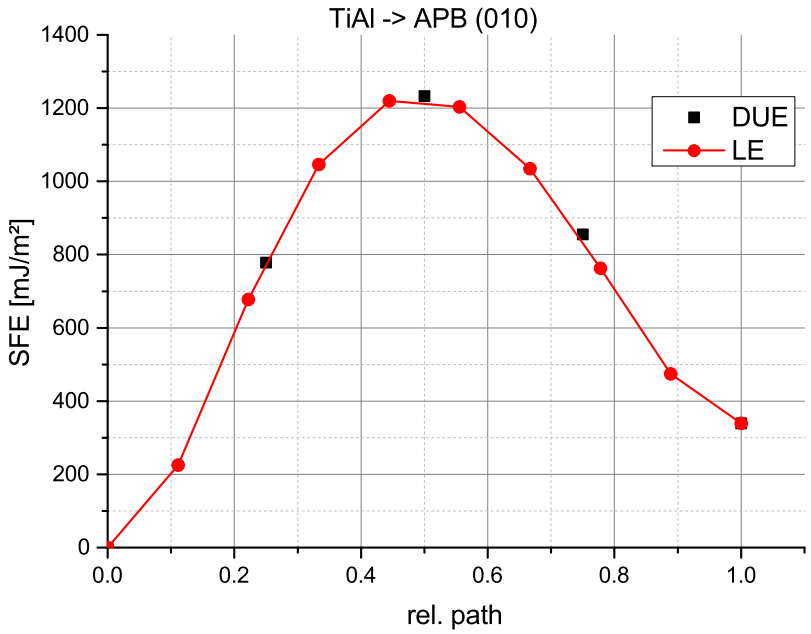

Figure 4.11: GSFE along the path from a perfect crystal to the APB(010). Rel. path corresponds to the fraction of the $\frac{1}{2}[101]$ direction. "DUE" points are relaxed along the [010] direction, "LE" along the supercell $\vec{b}$ direction.

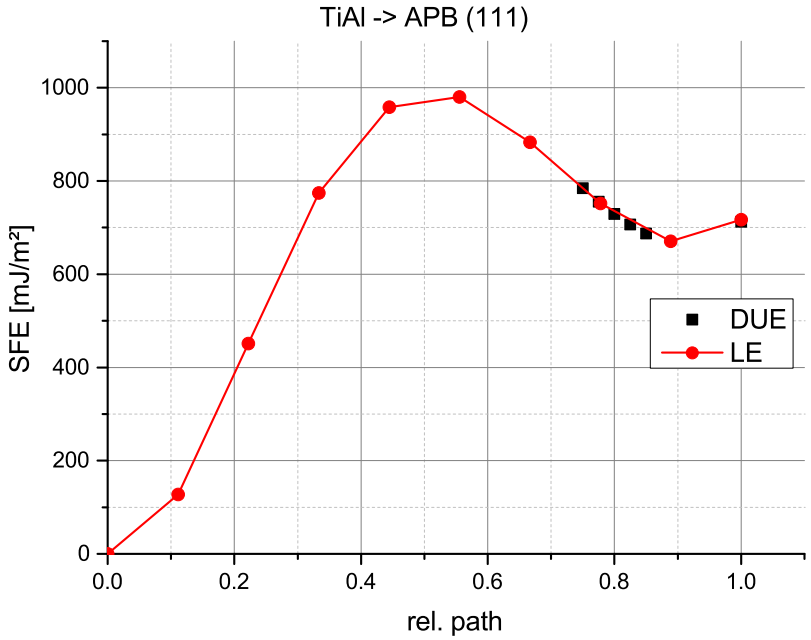

Figure 4.12: GSFE along the path from a perfect crystal to the APB(111), rel. path corresponds to fraction along the $\frac{1}{2}\left[01\bar{1}\right]$ vector. "DUE" points are relaxed along the direction [111], "LE" along the supercell $\vec{c}$ direction.

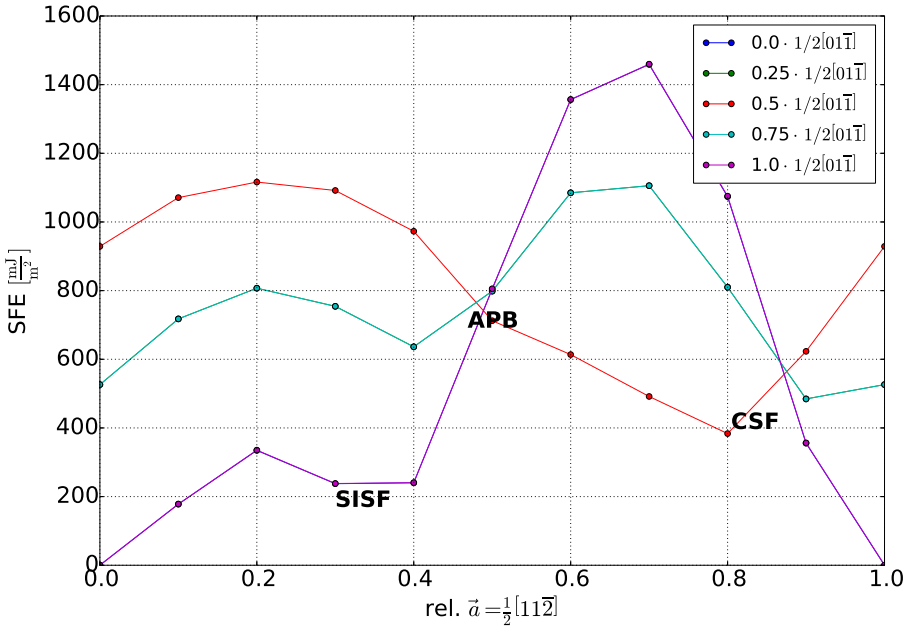

Figure 4.13: Cuts through the GSFE from Fig. 4.10. Labels indicate the position of particular fault.

Relaxation scheme

Until now, the relative positions of the atoms in the supercell were allowed to relax only along a single direction. To estimate the impact of this constraint, the following results were obtained with fully relaxed atoms (i.e. all three supercell direction were chosen to be the allowed relaxation directions). The results are summarized in Tab. 4.6.

The changes of the atom positions introduced by this relaxation scheme are in some cases complex and span over several distances of the (111) layers (Fig. 4.14).
The figure shows the APB for which the Ti atoms increase their spacing over the fault plane (layer in between the top plane, which is the periodic image of the first layer, and the one above), along the supercell $\vec{a}$ and supercell $\vec{c}$ directions, and that the Al atoms behave in the opposite sense, they decrease their spacing over the fault plane in the supercell $\vec{a}$ and $\vec{c}$ directions. This movement of the atoms is not possible to observe in the used scheme for

Table 4.6: SFE for freely relaxed atoms. Build-up of 4.2.3 used, previous calculated SFEs given for direct comparison. All values in $\left[\frac{mJ}{m^2}\right]$

SF	**$\vec{c}$ rel. dir.**	**free to move**
SISF	188	173
CSF	415	370
APB	717	635
twin	115	89

calculating the GSFE because they are only allowed to relax along one direction.

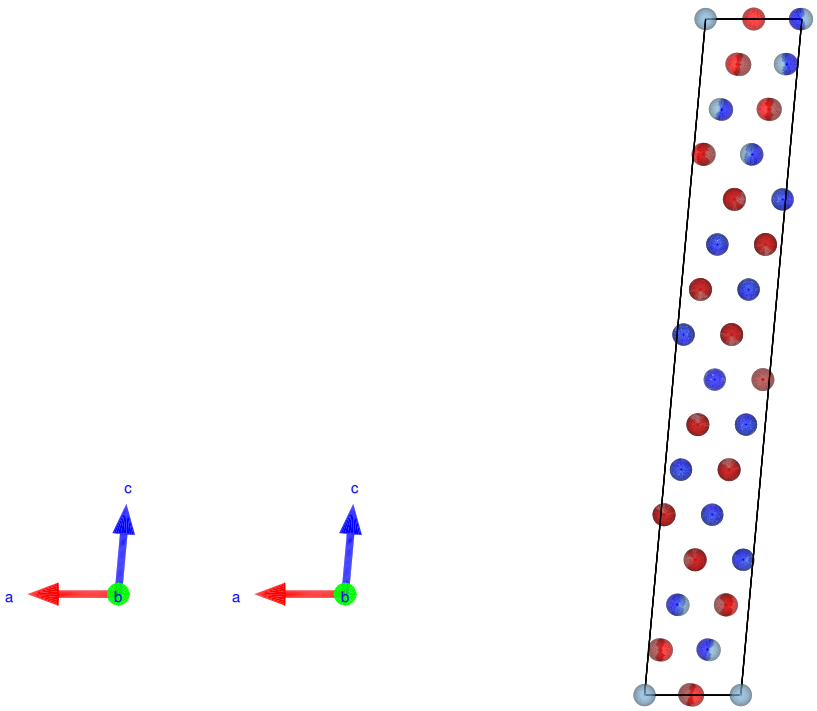

Figure 4.14: Overlaid picture of the supercell for calculating the APB(111) with $n = 15$ in the supercell $\vec{b}$ projection. Light blue and light red indicate the starting position of Al and Ti atoms respectively and their darker colored counter parts are the relaxed positions. When no movement occurs the initial positions are overlaid by the relaxed ones.

4.4.2 Real energy minimum of the GSFE

To have a better resolution in the vicinity of the exact hard-sphere stacking fault positions at the GSFE, a dense mesh was used to investigate the energy landscape along the $\frac{1}{6}\left[11\bar{2}\right]$ direction. The relaxation supercell $\vec{c}$ direction and $n = 15$ were applied. The results are presented in Figs. 4.15, 4.16 and 4.17. The data were interpolated with cubic polynomial functions also shown in the graphs. As already seen in the coarse mapping in Figs. 4.10 and 4.13 here is no local minimum found for the APB (see Fig. 4.15). The values of the fitted minimum for the CSF and the SISF are shown in Tab. 4.7.

4.4.3 Energy pathways

The energy pathways for several dislocation dissociation reactions have been calculated. Presented in Fig 4.18 is the reaction after Eq. 2.19 and in Fig. 4.19 after Eq. 2.15. Other energetic pathways balances can be constructed from these two graphs.

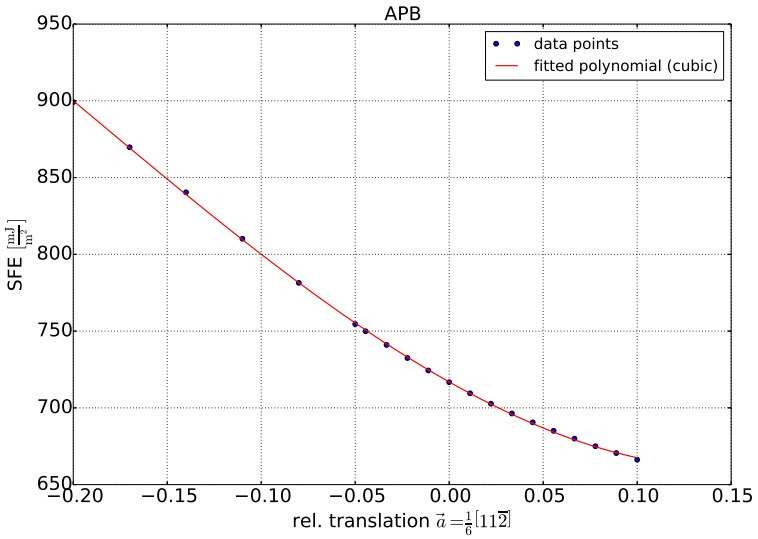

Figure 4.15: GSFE cut along the $1/6[11\bar{2}]$ direction in the vicinity of the APB. Zero relative translation indicates the hard-sphere position.

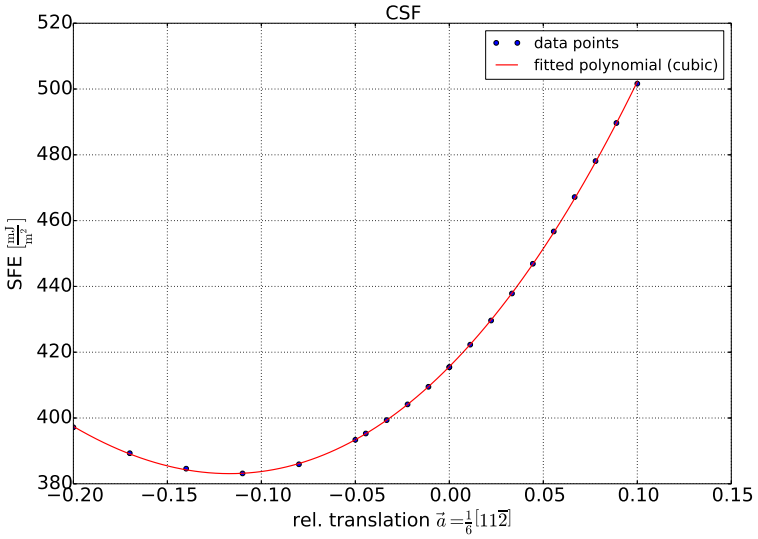

Figure 4.16: GSFE cut along the $[11\bar{2}]$ direction in the vicinity of the CSF. Zero relative translation indicates the hard-sphere position.

Additionally, the energy pathway from twin to twin has been investigated to determine the unstable twin energy γ_{ut}, similarly to the way implemented in [30]. The barrier energy was determined, through a polynomial fit of the fourth order, to be 359 $\frac{\mathrm{mJ}}{\mathrm{m}^2}$(see Fig. 4.20).

4.5 Results for the Molecular Dynamics

Due to the huge time saving potential of the MD, the GSFE of the stoichiometric γ-TiAl has been calculated also with LAMMPS. Two different EAM potentials were used [54, 55]. LAMMPS needs the supercell $\vec{a}$ defined along the global x-axis. In order to apply the

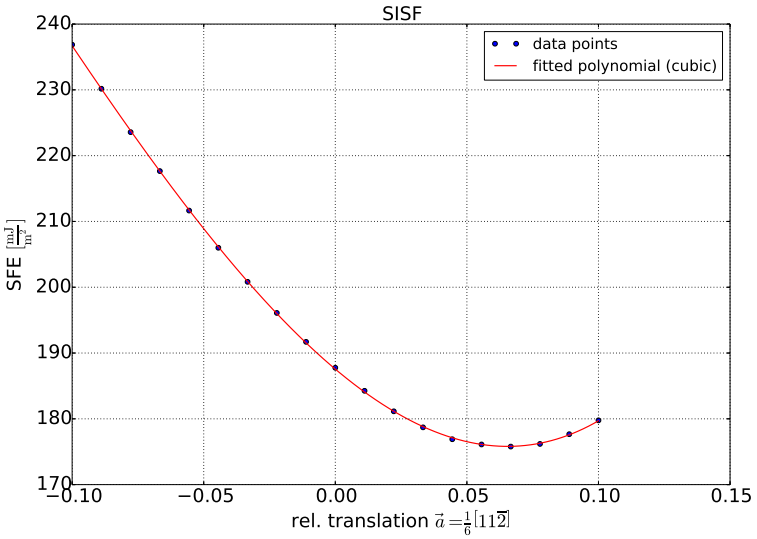

Figure 4.17: GSFE cut along the $[11\bar{2}]$ direction in the vicinity of the SISF. Zero relative translation indicates the hard-sphere position.

approach described in Sec. 4.2.3 with the relaxation direction parallel to [111], one needs to adjust the orientation of the supercell to the global coordinate system in a different way than for the DFT calculations. Beginning again with a supercell from Sec. 4.2.1, the supercell $\vec{a}$ is aligned along the x-axis through a rotation of the supercell with the procedure discussed in Sec. 4.4.1. Then, a second rotation of the cell along the supercell $\vec{a}$ direction, turns the supercell $\vec{c} = [111]$ direction into the global z-axis. The supercell $\vec{c}$ is then tilted away to build the fault through using the periodic boundary, as described in Sec. 4.2.3.
The relaxation is allowed only along the z-axis through fixing the forces in the x and y directions of the global coordinate system. The model consists of $n = 15$ layers with one plane containing 32 atoms. The atoms were relaxed to their equilibrium positions with the Polak-Ribiere version of the conjugate gradient scheme [45] with allowed stopping tolerance of force 10^{-10} [eV/Å].
The calculated GSFE are shown in Fig. 4.21, and a short summary of important values is given in Tab. 4.8.

It is clearly seen that for all three stacking faults, there exists a local minimum on the GSFE surface for both used potentials, but the observed energies differ in absolute values (see

Table 4.7: Stacking fault energies obtained from fitting the GSFE minimum positions.

SF	**rel. $\frac{1}{6}\left[11\bar{2}\right]$ translation**	**Min. GSFE**	Tab. 4.6
SISF	0.0653	176	173
CSF	-0.1168	383	370
APB	none	none	635

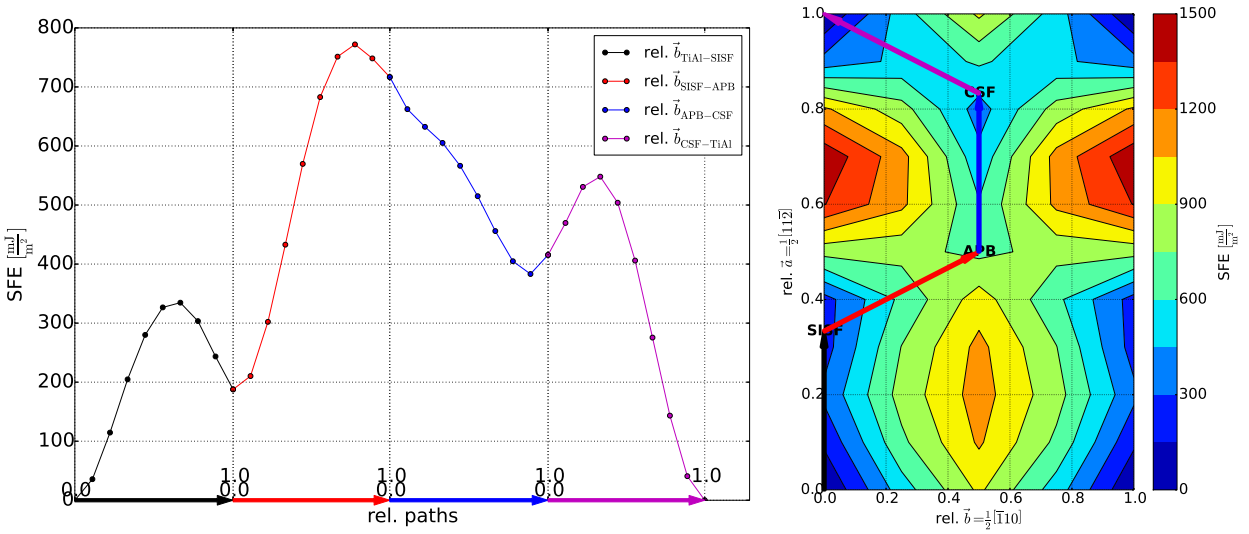

Figure 4.18: Energy profile along dissociation reaction according to Eq. 2.19. The analysed dislocation reaction is indicated in the GSFE contour plot.

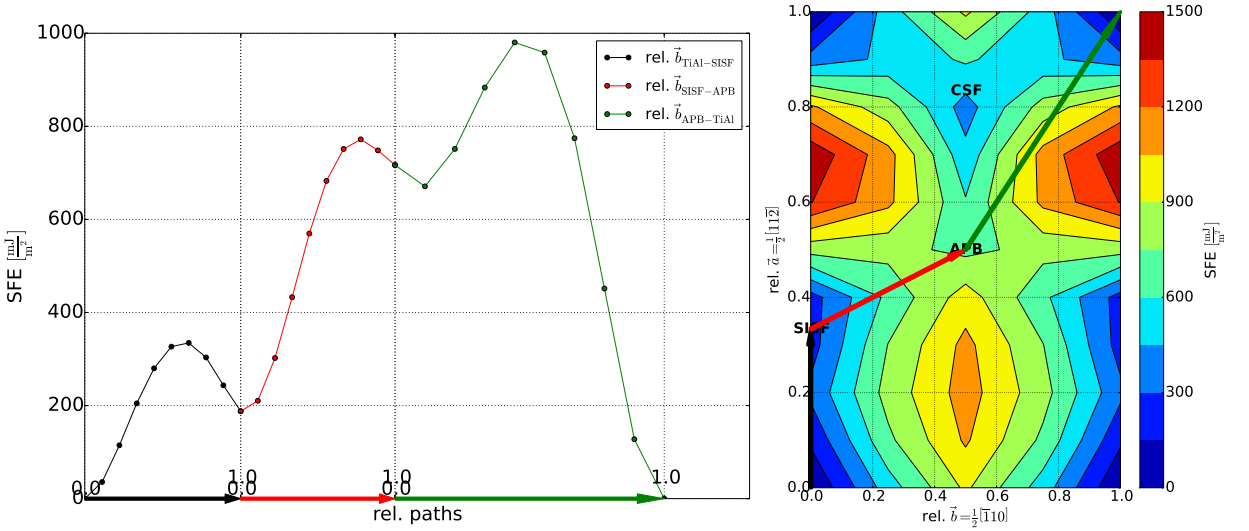

Figure 4.19: Energy profile along dissociation reaction according to Eq. 2.15. The analysed dislocation reaction is indicated in the GSFE contour plot.

Tab. 4.8), and result in different ordering. While the potential of Zope and Mishin [54] the stacking faults ordering is as 4.12

$$CSF > APB > SISF \tag{4.12}$$

and have higher energy barriers on the GSFE, the values calculated with the potential of Farkas and Jones [55] declare the hierarchy is the same as determined from the DFT method, and have generally lower barriers and a more non-spherical, strained shape of the barriers.

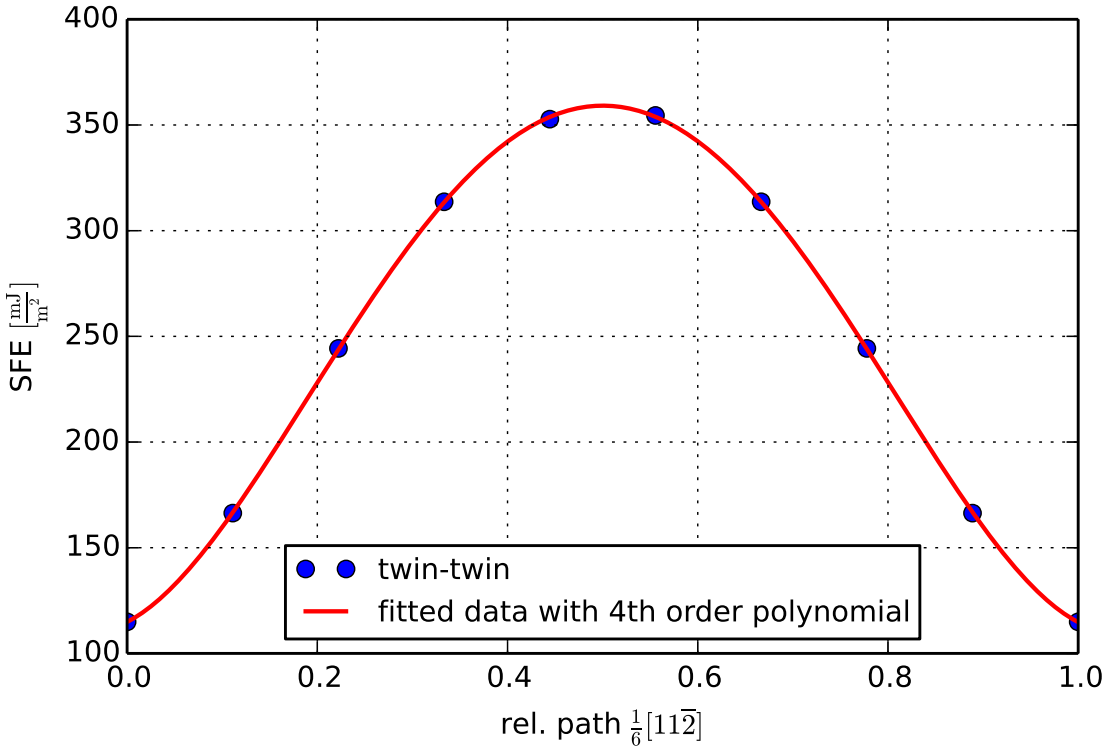

Figure 4.20: Energy profile from twin to twin. Twin geometry was implemented with $n = 12$, and relaxed along the supercell $\vec{c}$ direction.

4.6 Alloying Influence via DFT

To dilute the concentration of alloying elements in the fault plane the cross-section was extended to contain 4×2 atoms, i.e. the supercell $\vec{a}$ and $\vec{b}$ were doubled. To keep the calculation time reasonable, the number of layers n was reduced to $n = 6$, i.e. so that in the whole supercell contained 48 atoms.

Table 4.8: Stacking fault energies from MD calculations.

Potential	**hard-sphere pos.**	**minimum GSFE**
[54]		
APB	200	182
CSF	290	290
SISF	117	102
[55]		
APB	375	362
CSF	318	317
SISF	89	74

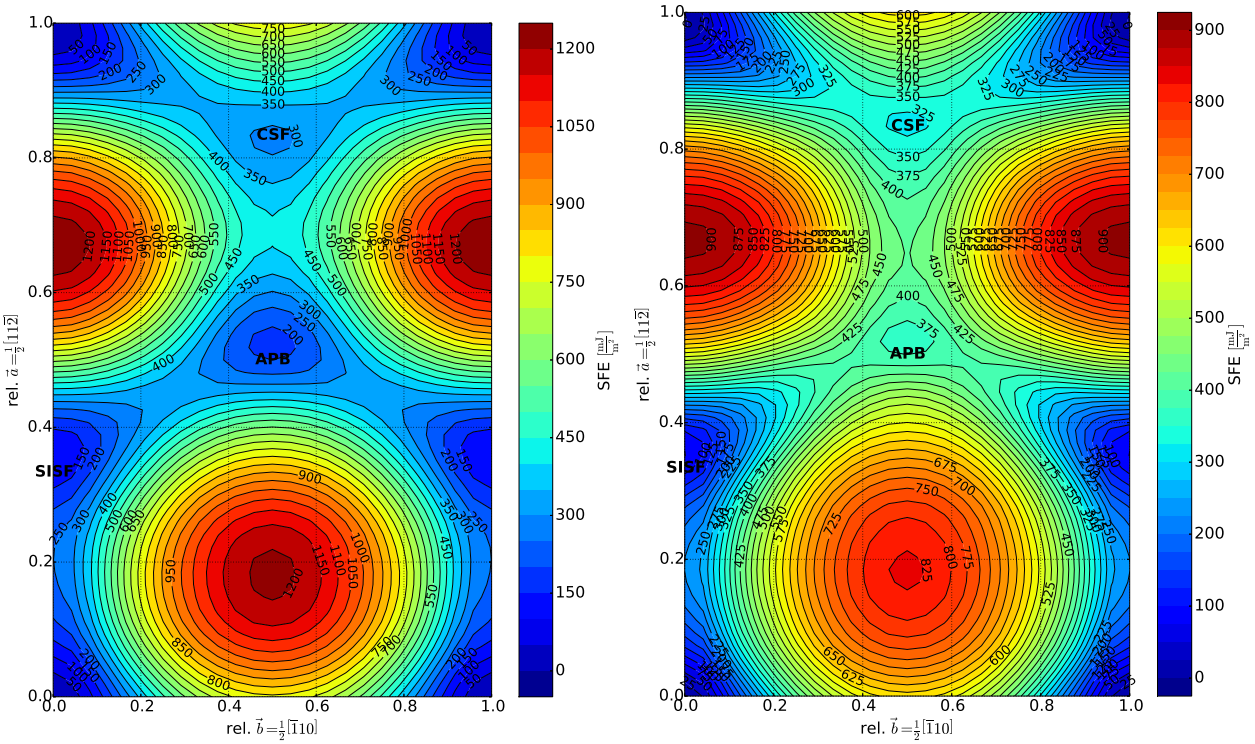

Figure 4.21: GSFE for the two different potentials. Left hand side the potential [54], right hand side the potential of [55].

An alloying element atom was placed at a plane neighboring with the fault. The alloyed γ-TiAl model is then fully relaxed with respect to the cell shape, volume and atomic positions. It should be noted that in contrast to the visualization in Fig. 4.22, all atoms are rigidly shifted by $\frac{1}{12}\vec{c}$ before applying the fault-producing displacement. This is a purely technical detail which, however, guarantees structural model of the planar faults. Subsequently the supercell $\vec{c}$ direction is modified to build the fault. The three fault producing vectors are:

$$\vec{b}_{\mathrm{APB}} = \frac{1}{4}\left(\vec{a}+\vec{b}\right), \tag{4.13}$$

$$\vec{b}_{\mathrm{SISF}} = \frac{1}{6}\vec{a}, \tag{4.14}$$

$$\vec{b}_{\mathrm{CSF}} = \vec{b}_{\mathrm{SISF}} - \vec{b}_{\mathrm{APB}}, \tag{4.15}$$

where $\vec{a}$ and $\vec{b}$ are the supercell lattice vectors of the alloying supercell.

A relation between the supercell concentration and a "real alloy" concentration is difficult, due to the limited supercell size and configuration. A lower limit for the "real" concentration is the concentration of the whole supercell, i.e., $\frac{1}{48}$ at.%. The upper limit is the concentration in the vicinity of the fault plane, i.e. $\frac{1}{16}$ at.%. It should be noted that the interaction of alloying elements across the fault plane could have significant influence. However, since all the alloying elements are treated the same way, this approximation still provides insight into the trends related to alloying.

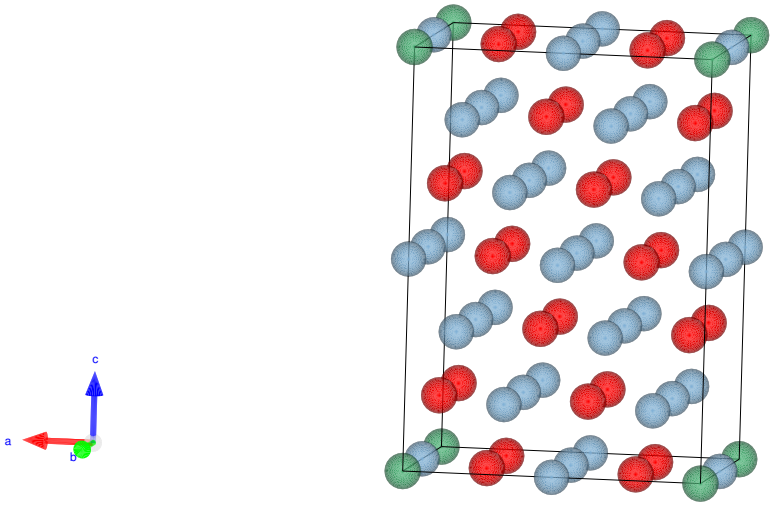

Figure 4.22: Alloying supercell, Ti atoms in red, Al atoms in light blue and the alloying element in green. Alloying element sits on Al position.

4.6.1 Influence of the alloying element to planar fault distance.

Owing to the constraints through the limited number of atoms in the supercell, the influence of where the alloying atom sits relative to the fault plane was investigated. The considered configurations are in Fig. 4.23.

Figure 4.24 gives the dependence of the SFE for SISF, CSF, and APB(111), for Ti-rich γ-TiAl, i.e. when 1 Al atom is replaced by 1 Ti atom. It can be concluded, that the influence of the alloying element is already shielded by two perfect layers between the fault and the alloying element.

4.6.2 Impact of ternary elements on Ti-rich TiAl

The impact of ternary elements on Ti-rich γ-TiAl has been investigated for Mo, V, Zr, Hf, Ta, Nb, W, Ti, and Cr. To achieve a Ti-rich environment in the vicinity of the fault the atomic arrangement shown in Fig. 4.25 was used. The alloying element X is put on a Ti site, and the Ti atom from this site is put on an Al site in the same plane. This arrangement is a consequence of an assumption that all chosen elements preferentially occupy Ti sites. The values predicted values are presented in Fig. 4.26. All values are calculated at the hard-sphere model positions, and the applied relaxation direction was the supercell $\vec{c}$ direction.

For all considered cases the APB drops significantly in comparison with the stoichiometric case. The CSF energy also decreases for all alloying elements, the most pronounced effect being obtained for Mo, V, W, Ti and Cr. The SISF is most influenced by Ti, and has similar

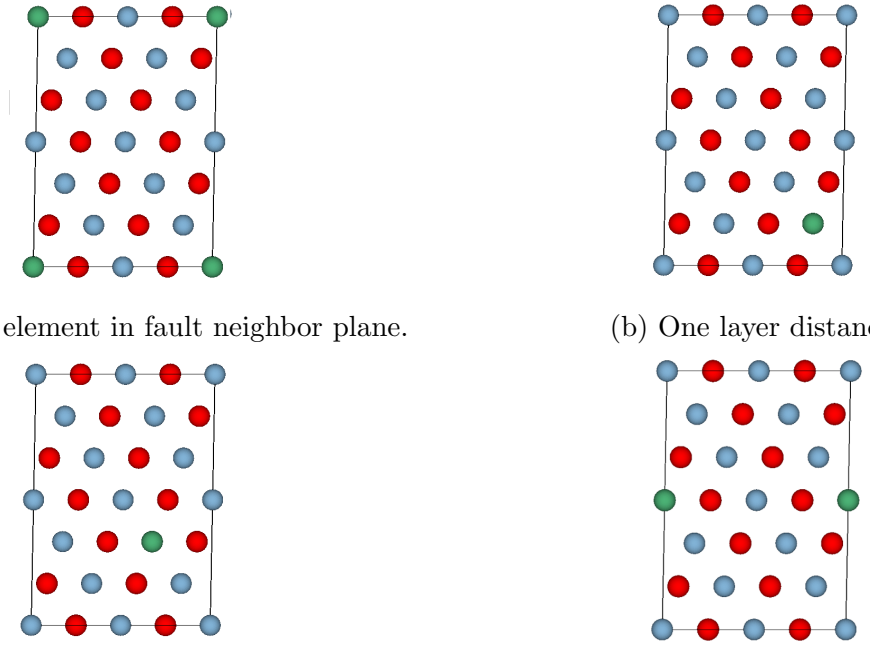

(a) Alloying element in fault neighbor plane.

(b) One layer distance.

(c) Two layers distance.

(d) Three layers distance.

Figure 4.23: Alloying supercells for different fault-alloying element spacing. Green is the alloying element, light blue are the Al atoms and red are the Ti atoms. In this sketch, the alloying element is exchanged with an Al atom.

values for all the other chosen alloying elements.

4.6.3 Impact of ternary elements on Al-rich TiAl

The effect of ternary elements in Al-rich alloys has been investigated only for Nb, the calculated results are reported in Fig. 4.27. The relaxation direction along the supercell $\vec{c}$ direction was used, and the fault values were investigated at the hard-sphere positions. the values for the stoichiometric TiAl with the standard lattice constants from Sec. 4.1 are given for reference.

The CSF and SISF energies are slightly increase from 415 to 429 $[\frac{\mathrm{mJ}}{\mathrm{m}^2}]$ and from 188 to 206 $[\frac{\mathrm{mJ}}{\mathrm{m}^2}]$, respectively, while APB decreases from 717 to 662 $[\frac{\mathrm{mJ}}{\mathrm{m}^2}]$ for alloying with Nb in the Al-rich concentration region.

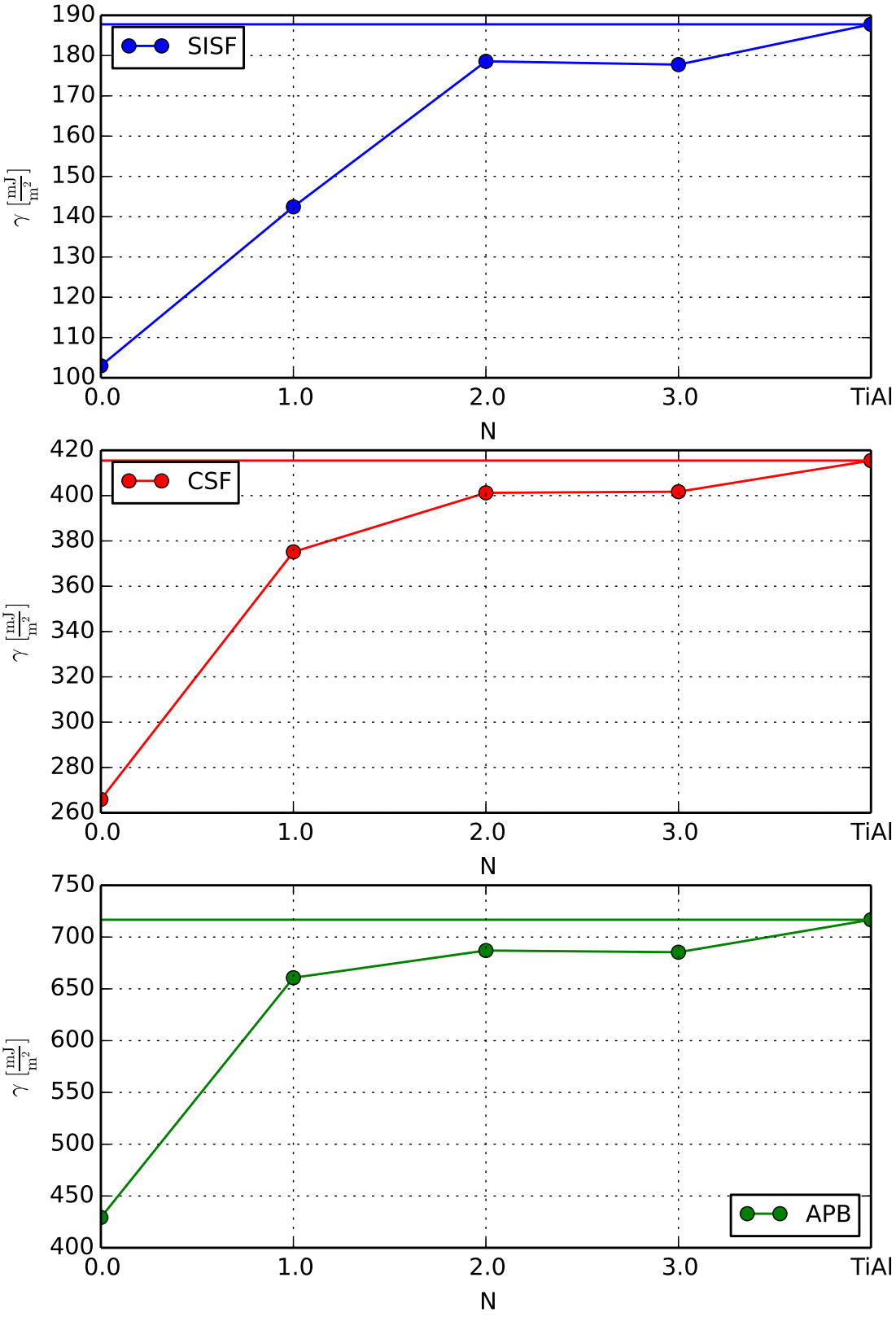

Figure 4.24: Influence of the fault-alloying element distance for X=Ti. N is the number of layers interspace separating the alloying element and the fault neighboring plane. Values for stoichiometric γ-TiAl are shown by the full horizontal line.

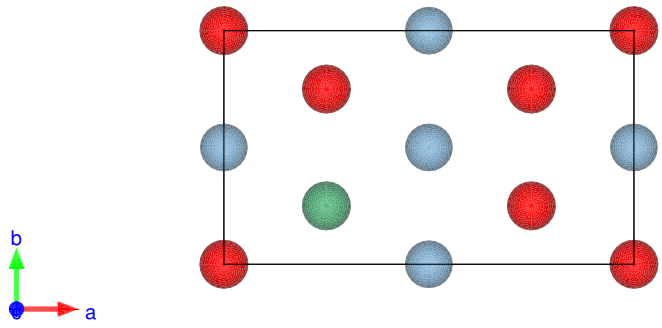

Figure 4.25: Arrangement of atoms in the plane neighboring the fault, shown in the [111] projection. The green sphere is the alloying element, red are the Ti atoms and light blue are the Al atoms.

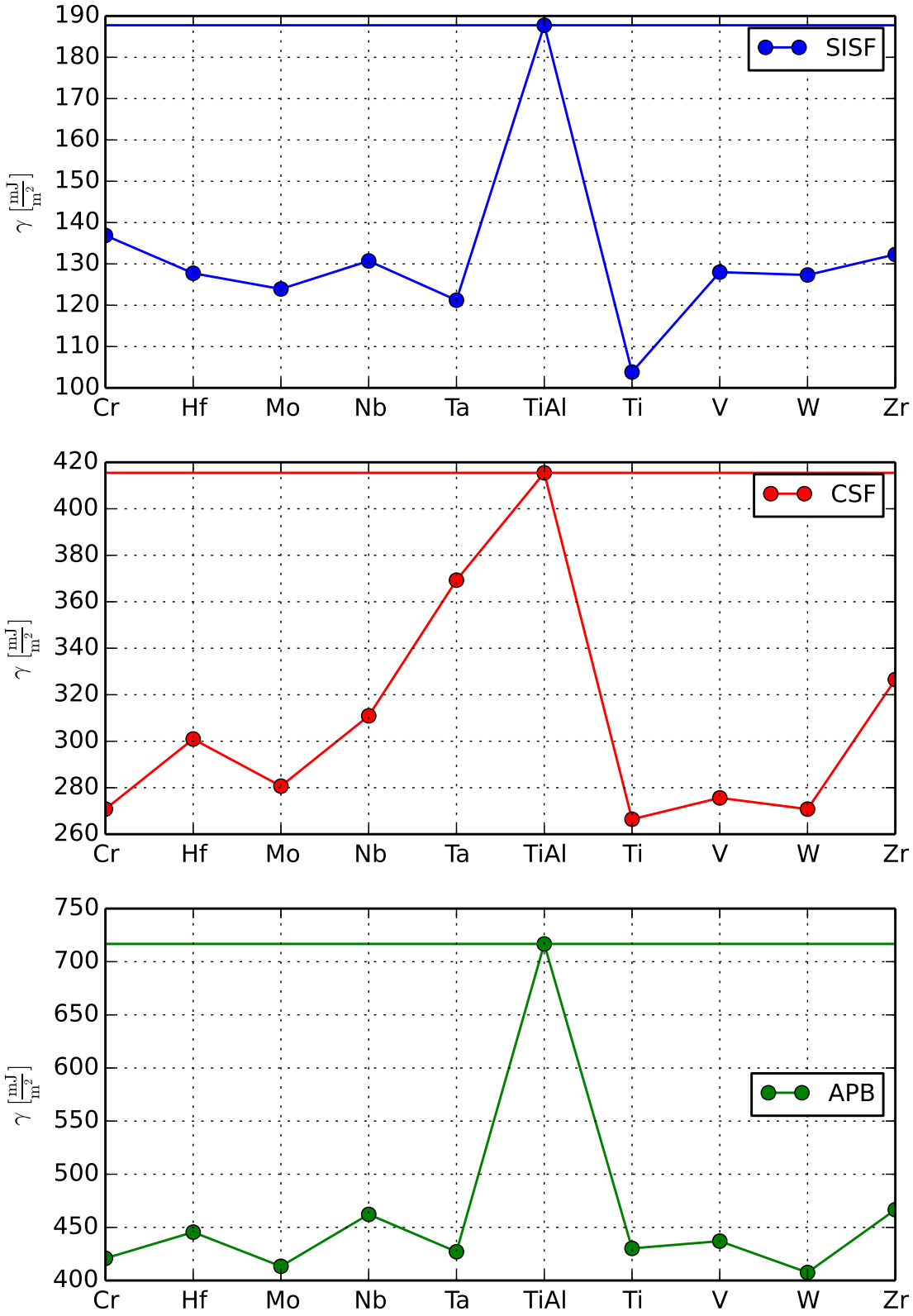

Figure 4.26: Impact of alloying element X in Ti-rich TiAl. The overall composition of the supercell was $Ti_{24}Al_{23}X_1$ in the whole supercell, while the fault neighboring layers have a composition of $Ti_8Al_7X_1$. Arrangement of atoms in the alloyed plane is shown in Fig. 4.25.

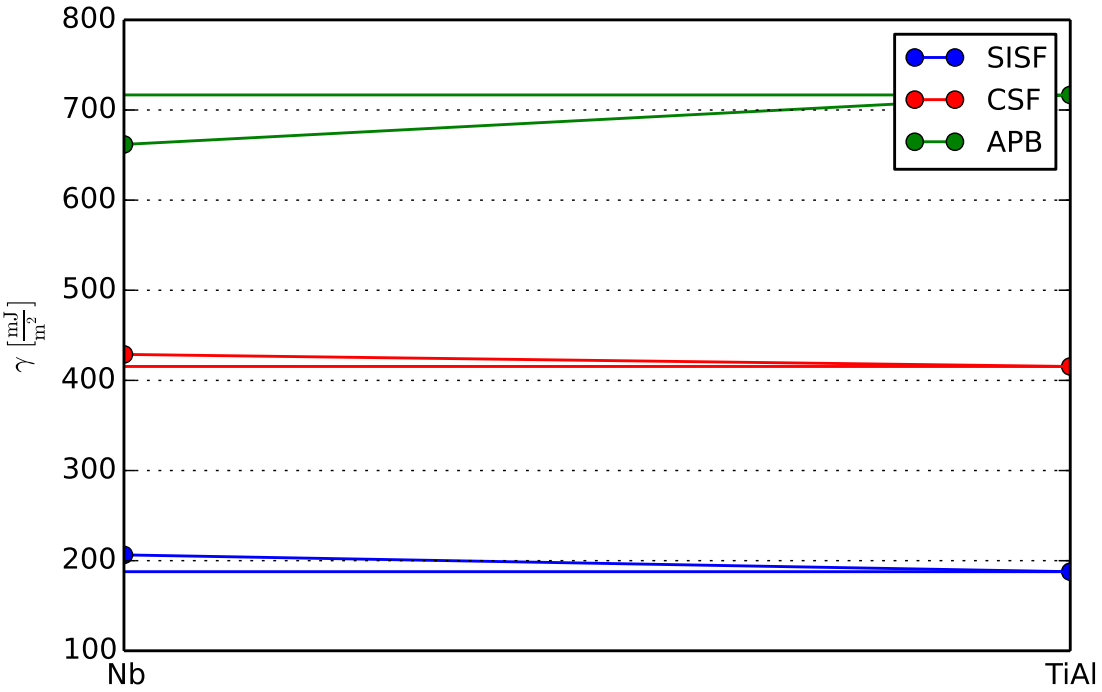

Figure 4.27: Impact of alloying elements in Al-rich TiAl. The overall composition of the supercell was $Ti_{23}Al_{24}X_1$ in the whole supercell, while the fault neighboring layers have a composition of $Ti_7Al_8X_1$. Alloyed atoms are exchanged with a Ti atom in the alloyed plane.

Chapter 5

Summary and discussion

In this Master Thesis the build-up of the geometries for different planar faults in γ-TiAl SISF, APB, CSF, SESF, twin and APB(010) was discussed. Two different methodologies to build the stacking faults were applied: the displacement geometries Sec. 4.2.2 and the pseudo-shear approach Sec. 4.2.3. These different build-ups were compared and showed to exhibit good agreement to each other (Sec. 4.3). The ordering $APB > CSF > APB(010) > SISF$ was obtained from our *ab initio* calculations.

The study of different exchange-correlation potentials showed that the LDA the values for the SISF, CSF and APB are lower than when GGA is applied (Sec. 4.3.1).

Further, the effect of different cell volumes was investigated (Sec. 4.3.2) and the equilibrium lattice constants were examined in Sec. 4.3.3. The SISF, CSF and APB energies increase with decreasing cell volume, and decrease with larger cell volumes, though the influence for the SISF is very small. The standard lattice constants as used in this thesis were found to correspond to a lattice under hydrostatic pressure.

The influence for different relaxation directions and schemes was also studied. For supercells with a number of layers, $n = 15$, the influence of the relaxation direction was found to be negligible. When the atoms were fully relaxed significant lower values than those for the hard-sphere model positions were obtained.

The GSFE was calculated for the (111) plane (Sec. 4.4) and detailed for several profiles corresponding to dislocation dissociation reactions, the twin to twin path and the energy pathway for the APB(010). The largest energy barrier was found on the way from SISF to the APB on the (111) plane. For the paths along the cell vectors, the energy barrier on the ordinary dislocation direction $\frac{1}{2}[\bar{1}10]$ is lower than on the superdislocation direction $\frac{1}{6}[11\bar{2}]$, which corresponds to the global maximum on the GSFE. The barriers for the straight lines from the perfect cell to APB(111) and APB(010) were calculated yielding that a larger barrier has to be overcome for the APB(010). The real energy minimum for the SISF and CSF were found to differ from the hard-sphere model positions. No local minimum was found along the $\frac{1}{6}[11\bar{2}]$ direction for the APB.

The GSFE of the (111) plane was calculated using the MD program LAMMPS for two different potentials. The values differ from the DFT predictions. For one of the potentials, the ordering of the SFE is different to that of the *ab initio* calculations. Generally, all SFE (APB, CSF and SISF) have lower values, and correspond to local minimum on the GSFE. Energy minimum positions are again different from their hard-sphere model positions of the faults.

Finally, the alloying influence was investigated using DFT for the three faults on the (111) plane. The calculations were divided into two groups, yielding the Ti-rich and the Al-rich compositions. The elements were assumed to occupy Ti sites. The stacking fault energies were observed to strongly depend on the $\frac{\mathrm{Ti+X}}{\mathrm{Al}}$ ratio. The SISF, CSF and APB energies decrease for ternary additions in a Ti-rich region in the vicinity to the fault. While the SISF and CSF increase for ternary additions in a Al-rich region in the vicinity to the fault, the APB slightly decreases. For the SISF energy, the influence was largest when the "ternary" alloying element was X = Ti. It should be noted, that the values for the "hard-sphere model positions" are discussed in this section, and the real energy minimum may give a slightly different picture in the hierarchy of the influence of a particular element.

Chapter 6

Outlook

The future work should include the evaluation of GSFE and the stacking faults for the DFT equilibrium constants. For the stacking fault energies and the calculations for investigating the impact of alloying elements on the stacking fault energies, the relaxation scheme for fully relaxed atoms will be a fine adjustment for seeing trends more clearly.
The twin to twin energy-profile will give prediction of critical twin stresses for different alloying elements. Further work will include the general way to investigate alloying effects via DFT by the further development of the LKKR-CPA and/or the SQS methods.
A big step will be to examine the influence of temperature on the stacking fault energies which had been neglected throughout this thesis, despite a rough approximation via volume expansion. The MD with an accurate potential is an attractive candidate to investigate the temperature and off-stoichiometric effects. To get alloying trends under consideration finite temperature DFT calculations will be needed.
On the experimental side, there are several possibilities to investigate effects regarding stacking fault energies. Measuring the partials separations in the TEM on model alloys for chosen alloying agents could be used to confirm the alloying influence on the stacking fault energies. Diffraction methods, the atom location channeling enhanced microanalysis (ALCHEMI), as well as atomic probe tomography (APT) are options to investigate the site occupancy of the elements which influences the SFEs. The local chemistry effects (Suzuki effect) should be also possible to be observed with the APT, the EDS and electron energy loss spectroscopy (EELS) within the TEM.

As David Hilbert once said:

> "**We must know — we *will* know!**"

Bibliography

[1] H. Clemens, BHM Berg- und Hüttenmännische Monatshefte **153**, 337 (2008).

[2] H. Clemens and S. Mayer, Advanced Engineering Materials **15**, 191 (2013).

[3] D. Dimiduk, Materials Science and Engineering A **263**, 281 (1999).

[4] F. Appel, J. D. H. Paul, and M. Oehring, eds., *Gamma Titanium Aluminide Alloys* (Wiley-VCH, Weinheim, 2011).

[5] J. Hirth and J. Lothe, *Theory of dislocations* (McGraw-Hill, New York, 1968).

[6] E. Tadmor and N. Bernstein, Journal of the Mechanics and Physics of Solids **52**, 2507 (2004).

[7] G. Gottstein, *Physikalische Grundlagen der Materialkunde* (Springer-Verlag, Berlin, 2007).

[8] M. Yoo, Intermetallics **6**, 597 (1998).

[9] G. Hug, A. Loiseau, and P. Veyssiere, Philosophical Magazine A: Physics of Condensed Matter, Structure, Defects and Mechanical Properties **57**, 499 (1988).

[10] H. Kestler and H. Clemens, *Titanium and Titanium Alloys*, edited by C. Leyens and M. Peters (WILEY-VCH,, Weinheim, 2003) p. 351.

[11] J. Schuster and M. Palm, Journal of Phase Equilibria and Diffusion **27**, 255 (2006).

[12] G. L. Chen, W. J. Zhang, Z. C. Liu, S. J. Li, and Y.-W. Kim, Gamma Titanium Aluminides **371** (1999).

[13] S. Znam, *BOND ORDER POTENTIALS FOR ATOMISTIC STUDIES OF DISLOCATIONS AND OTHER EXTENDED DEFECTS IN TiAl*, Ph.D. thesis, University of Pennsylvania (2001).

[14] J. Ehmann and M. Fähnle, Philosophical Magazine A: Physics of Condensed Matter, Structure, Defects and Mechanical Properties **77**, 701 (1998).

[15] Y. Wen and J. Sun, Scripta Materialia **68**, 759 (2013).

[16] V. Vitek, K. Ito, R. Siegl, and S. Znam, Materials Science and Engineering A **239-240**, 752 (1997).

[17] Y. Liu, L. Liu, S. Wang, and H. Ye, Intermetallics **15**, 428 (2007).

[18] M. Kanani, A. Hartmaier, and R. Janisch, Intermetallics **54**, 154 (2014).

[19] G. Hug, J. Douin, and P. Veyssiere, Materials Research Society Symposium Proceedings **133**, 125 (1989).

[20] J. P. Simmons, S. I. Rao, and D. M. Dimiduk, Materials Research Society Symposium - Proceedings **288**, 335 (1993).

[21] J. M. K. Wiezorek and C. J. Humphreys, Scripta Metallurgica et Materiala **33**, 451 (1995).

[22] M. A. Stucke, V. K. Vasudevan, and D. M. Dimiduk, Materials Science and Engineering A **192-193**, 111 (1995).

[23] M. Asta and A. Quong, Philosophical Magazine Letters **76**, 331 (1997).

[24] C. Woodward and J. Maclaren, Philosophical Magazine A: Physics of Condensed Matter, Structure, Defects and Mechanical Properties **74**, 337 (1996).

[25] R. Mahapatra, A. Girshick, D. Pope, and V. Vitek, Scripta Metallurgica et Materiala **33**, 1921 (1995).

[26] W. J. Zhang and F. Appel, Materials Science and Engineering A **334**, 59 (2002).

[27] Y. Yuan, H. Liu, X. Zhao, X. Meng, Z. Liu, T. Boll, and T. Al-Kassab, Physics Letters, Section A: General, Atomic and Solid State Physics **358**, 231 (2006).

[28] M. Duesbery and V. Vitek, Acta Materialia **46**, 1481 (1998).

[29] V. Vitek, Cryst Lattice Defects **5**, 1 (1974).

[30] S. Kibey, J. Liu, D. Johnson, and H. Sehitoglu, Acta Materialia **55**, 6843 (2007).

[31] E. Tadmor and S. Hai, Journal of the Mechanics and Physics of Solids **51**, 765 (2003).

[32] S. Mahajan and G. Chin, Acta Metallurgica **21**, 1353 (1973).

[33] J. Friedel, *Dislocations* (Addison-Wesley, Reading, MA, 2002).

[34] J. C. M. Li, Acta Metallurgica **8**, 563 (1960).

[35] D. Roundy, C. Krenn, M. Cohen, and J. Morris Jr., Physical Review Letters **82**, 2713 (1999).

[36] F. Kuypers, *Klassische Mechanik* (Wiley-VCH, Weinheim, 2010).

[37] J. Lee, *Computational Materials Science* (CRC-Press, Boca Raton, 2010).

[38] S. Cottenier, Instituut voor Kern-en Stralingsfysica, KU Leuven, Belgium (2002).

[39] D. Holec, *Multi-scale modelling of III-nitrides: from dislocations to the electronic structure*, Ph.D. thesis, University of Cambridge (2008).

[40] P. Hohenberg and W. Kohn, Physical Review **136**, B864 (1964).

[41] W. Kohn and L. Sham, Physical Review **140**, A1133 (1965).

[42] J. Perdew, K. Burke, and M. Ernzerhof, Physical Review Letters **77**, 3865 (1996).

[43] G. Kresse and J. Furthmüller, Physical Review B - Condensed Matter and Materials Physics **54**, 11169 (1996).

[44] G. Kresse, M. Marsman, and J. Furthmüller, *VASP the GUIDE* (2014).

[45] *LAMMPS Users Manual* (2014).

[46] S. Plimpton, Journal of Computational Physics **117**, 1 (1995).

[47] K. Momma and F. Izumi, Journal of Applied Crystallography **44**, 1272 (2011).

[48] F. Murnaghan, Proceedings of the National Academy of Science **30**, 244 (1944).

[49] F. Birch, Physical Review **71**, 809 (1947).

[50] E. Jones, T. Oliphant, P. Peterson, *et al.*, "SciPy: Open source scientific tools for Python," (2001–).

[51] J. D. Hunter, Computing In Science & Engineering **9**, 90 (2007).

[52] Z. Pei, L. Zhu, M. Friák, S. Sandlöbes, J. Von Pezold, H. Sheng, C. Race, S. Zaefferer, B. Svendsen, D. Raabe, *et al.*, New Journal of Physics **15**, 043020 (2013).

[53] K. Meyberg and P. Vachenauer, *Höhere Mathematik 1* (Springer-Verlag, Berlin, 2013) p. 319.

[54] R. Zope and Y. Mishin, Physical Review B - Condensed Matter and Materials Physics **68**, 241021 (2003).

[55] D. Farkas and C. Jones, Modelling and Simulation in Materials Science and Engineering **4**, 23 (1996).